2008

Shaping Graphene: An Alternative Approach

Ian W. Frank
Pomona College

Shaping Graphene

An Alternative Approach

Ian Frank

May 7, 2008

Abstract

With experimentation on graphene (an atomic layer of graphite) becoming more and more common it is imperative that we have the capability to shape the material beyond the random manner in which it is deposited by mechanical exfoliation. This capability would be invaluable not only for the interesting electronic and optical properties that can be obtained, but also potentially for characterizing the mechanical resonators that we have been able to fabricate here at Pomona College by suspending few-layer graphene sheets over trenches in SiO_2. We propose novel methods for etching graphene that should allow us to shape the material when used in conjunction with our e-beam lithography capabilities.

Contents

Chapter 1

Introduction

1.1 What is graphene?

Imagine a benzene ring: a planar, hexagonal array of carbon and hydrogen atoms. Now imagine that instead of terminating each carbon atom with a hydrogen atom, you connected it to another hexagonal array of carbon atoms. Because of the angles involved, you can, in a flat plane, construct a sheet of infinite hexagons - just sp^2 bonded carbon atoms as far as the eye can see (Figure 1.1). This would constitute a truly two-dimensional world with wondrous properties: this is the world of graphene. Graphite is a material that most people are familiar with, but what most people do not realize is that graphite is simply millions upon millions of graphene sheets stacked one on top of the other; subsequently by removing the top few layers it is possible isolate graphene or few-layer graphene sheets. Although graphene must have existed since the time people started using graphite as pencil lead, it was not "seen" until very recently, and graphene was viewed as a theoretical playground with wondrous properties that could be calculated but never utilized or experimented upon. Then a few years ago some researchers found that by rubbing graphite across a dielectric of appropriate thickness, sheets of graphene lying around would become visible[1, 2], allowing

us to see the atomically-thin sheets that must have been lying on the surface of every piece of paper that we have ever written on with our graphite pencils.

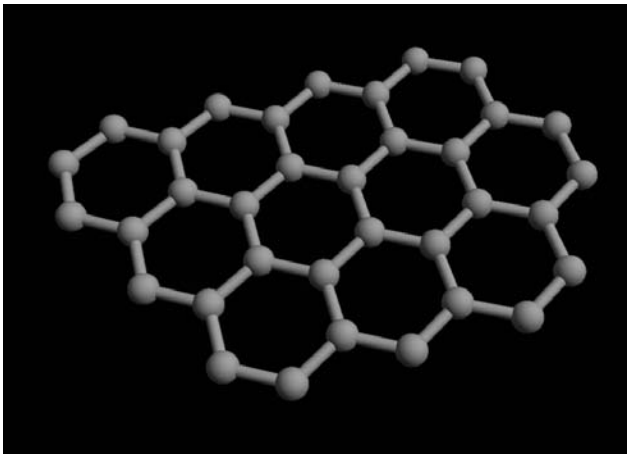

Figure 1.1: *A 3-D model of sp-2 bonded planar carbon or: graphene*

Once it was confirmed that graphene could be reproducibly found on a silicon dioxide wafer, a torrent of experiments quickly followed, and renewed interest has led to a multitude of theoretical predictions and exotic experiments utilizing graphene's unique properties. For instance electrons behave in strange ways when they are confined to graphene. The electrons are essentially ballistic, referred to as Dirac Fermions, they travel freely through the atomic lattice as if they had no mass. This results in an extremely high conductance with charge carriers that can be both positive or negative depending on applied electric fields[3]. The two dimensional nature of the substance also means that it is ideal for the Quantum Hall Effect, and because of the nature of the Dirac Fermions, the Quantum Hall Effect is observed at room temperature[4, 5] while in other, more conventional, materials liquid helium temperatures are required to observe the same behavior. In addition to its electronic properties graphene is also extremely strong and stiff for its dimensions, with a very high Young's modulus. This potentially means that mechanical resonators consisting of graphene would be excellent for detecting mass and charge in very low quantities[6].

Graphene could also revolutionize the way computer chips are made. Because of its incredible properties of electron transport that vary with the lattice orientation, and high conductance, the material could be used to implement resistors, transistors, and interconnects[7]. Because of its amazingly small thickness it also exhibits the "electric field effect" despite its

record setting carrier mobilities[3, 8]. In a normal conductor external electric fields are shielded out past a skin depth on the order of $1nm$; thus applied gate voltages do not affect the conductance of the material. For this reason we must use semiconductors in the channels of transistors so that they can be turned "on" and "off." Because it is one atomic layer thick graphene does not shield out external fields and thus its resistance can be raised through use of an applied gate voltage. Looking further into the future we see that graphene should be able to support electromagnetic waves propagating through its plane[9]. The frequency of these waves should be tunable over a large range leading to speculation that light could be confined to nanoscale structures on chips, propagating with low losses, and so laying the ground work for photons displacing electrons in computing.

1.2 The Importance of Shaping Graphene

1.2.1 Random Deposition and Standard Processing

While alternative methods such as chemical vapor deposition (CVD) are starting to emerge [10, 11], the most common method for obtaining graphene is still by mechanical exfoliation[12]. This is a highly unpredictable process that scatters the thinnest sheets of graphite all over a surface of an SiO_2 wafer, with no way of pre-determining their shape or the orientation of the crystal lattice. A sample of graphene can be seen in figure 1.2. Even in these ideal conditions on top of $100nm$ of SiO_2 it is very difficult to make out. While efforts can be made to alter the surface of the wafer that the sheets are deposited on, usually the best that this will do is cause some kind of localization of the graphene sheets[6], but their size and shape is still almost random. For some of the earlier experiments this was not a problem. Electrodes could be placed arbitrarily so that many transport measurements could be carried out. Additionally the natural variation in size and thickness was useful for our mechanical experiments because we were able to determine if properties, like effective spring constants,

scaled according to our theoretical predictions[6, 13].

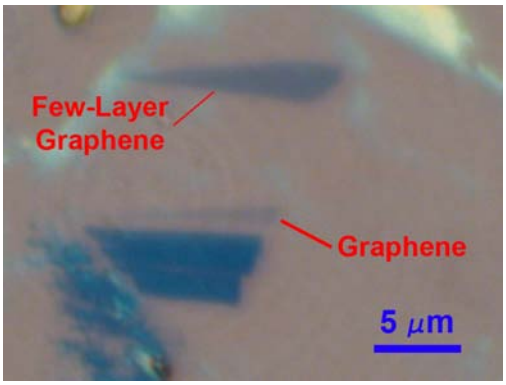

Figure 1.2: *Graphene and few-layer graphene on an SiO_2 wafer. The darker, unlabeled, material is thicker graphite and glue residue. Notice that the shape is irregular and random.*

With the later generation, more sophisticated, experiments more precision and control over shapes and sizes of the sample is necessary. Because we cannot dictate how the graphene is deposited we must use well established techniques for patterning and etching to achieve important shapes like Hall crosses (see figure 1.5 for an example of a graphene Hall cross) or even the more refined shapes that are theoretically predicted to act as circuit elements or wave guides[4, 7, 14](See figure 2.4).

One tried and true method for patterning graphene is to use electron-beam lithography to create masks that have feature sizes that can be as low as $10nm$ or less. Once these masks are developed the sample would then be placed in a simple reactive ion etcher (RIE) where an oxygen plasma would quickly and easily etch away any of the exposed carbon. A quick exposure to more chemicals would then remove the mask, leaving behind the graphene in the shape of the mask. While the e-beam lithography can be tricky, at most major institutions with nano-fabrication capabilities this process would be relative simple compared to some of the multi-step processes regularly performed, and the thrust of this project was to develop such capabilities here at Pomona. Once the graphene is in the desired shape it will be available to add any other features such as electrodes or antennas to allow photons or electrons to be coupled into the graphene.

1.2.2 The Quantum Hall Effect (QHE) and Hall Crosses

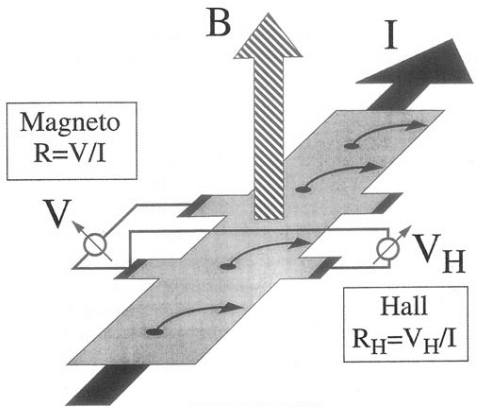

Figure 1.3: *This schematic of the Hall experiment is taken from Horst L. Störmer's 1998 Nobel lecture on the fractional quantum Hall effect.*

The Hall effect is a fairly simple method of determining the sign of charge carriers in a material where electricity is conducted. The nature of the Lorentz force, (equation 1.1), means that charged particles moving perpendicular to a magnetic field in the absence of an electric field will start to precess and eventually exhibit uniform circular motion. If an electric field is parallel to the initial velocity then, as we can see from equation 1.1, the particle will still be pushed in the direction of $\vec{E}$ and the long term motion will be more of a spiral in a plane. The Lorentz force is given by

$$\vec{F} = q(\vec{E} + \vec{v} \times \vec{B}). \tag{1.1}$$

Where $\vec{F}$ is the force, q is the charge of the particle, $\vec{v}$ is the velocity, and $\vec{E}$ and $\vec{B}$ are the electric and magnetic fields respectively. Now given this force law, if we were to setup a conductor with current running through it, achieved by a parallel electric field, and then set up a perpendicular magnetic field to the plane of the conductor as pictured in figure 1.3, then depending on the sign of the charge carriers there will be a build up of the charged particles on one side or the other. A transverse measurement of the voltage will determine the sign of the carriers. This voltage does not build up indefinitely as the increased concentration of charge will repel like charges. Thus we find that the Hall voltage will depend on the current and the strength of the applied magnetic field.

The 1985 Nobel Prize was awarded to Klaus von Klitzing for observing the quantized Hall effect. Using molecular beam epitaxial growth he created a two dimensional electron gas (2-DEG) in a $GaAs$ structure, that when lowered to liquid He temperatures exhibited behavior very different from the regular Hall effect. Instead of a continuous increase of the Hall voltage as the magnetic field was increased, he noticed that the voltage went up in quantized steps related to the electron charge and Planck's constant. This is because electrons are fermions and therefore cannot occupy the same quantum state. Thus if we consider the electrons precessing in the perpendicular magnetic field to be in quantized states, a given radius can only contain so many electrons, depending on the degeneracy of the state. These so called Landau levels can contain a number of electrons proportional to the magnetic field. Therefore as the magnetic field is lowered, electrons are forced to jump to higher Landau levels, when this jump occurs the magneto (as labeled in 1.3) momentarily drops as more electrons are allowed to cross the Hall setup. But once the levels are again filled, no more electrons can propagate through, and the resistance increases. The transverse resistance takes on integer multiples of $h/(ie^2)$ where h is Planck's constant, e is the electron charge, and i can be any positive integer. The transverse resistance, or Hall resistance, became the standard for defining the Ohm (Ω) in 1990 because it was found to be quantized over broad ranges to better than a few parts per billion and can be reproducibly measured to eight significant figures. Oddly enough it turns out that this effect relies not only on the quantum effects but also on the impurities in the 2-DEG.

In 1998 Horst L. Störmer, Daniel C. Tsui, and Robert B. Laughlin were awarded the Nobel prize in Physics for their discovery of "a new form of quantum fluid with fractionally charged excitations." Störmer and Tsui first observed this effect in 1981 when they made Hall measurements on extremely pure $GaAs$ structures that yielded quantized steps that were fractional rather than integer steps of h/e^2. Laughlin later developed the theoretical structure to explain this behavior. The fractional steps were startling because they described

particles with a charge less than $|e|$ which was previously unseen outside of quarks in high energy experiments. The actual details of this effect are far too complex to discuss here, however, I will attempt to give a broad overview of the physics involved.

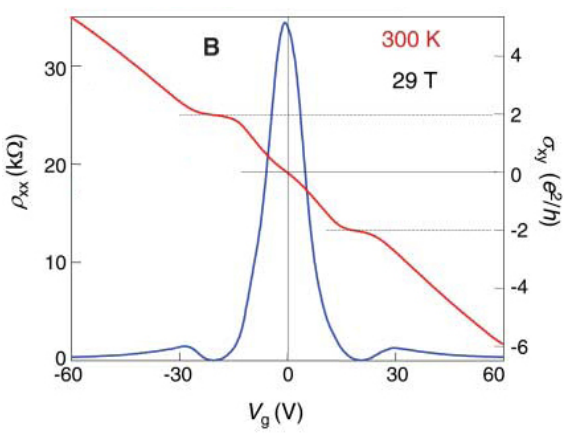

Figure 1.4: *This image was adapted from Novoselov's paper on the observation of the QHE at room temperature[5]. σ_{xy}, or the transverse conductivity, clearly levels off at values of $\pm 2e^2/h$, corresponding to a Hall resistance of $h/2e^2$.*

The main idea is that for the integral quantum Hall effect (IQHE) electrons each occupy their own states and do not really interact with each other. To understand the fractional quantum Hall effect (FQHE) you must consider a many particle system. The FQHE is observed in the magnetic fields where the IQHE Landau levels are partially full. This means that electrons can spread out to avoid each other. It is one of the peculiarities of solid state physics that electron-electron interactions become *more* significant as their density decreases. Because of the applied magnetic field inside the material there are tiny current vortices called flux quanta. Each flux quantum accounts for a magnetic flux of h/e, so the number of quanta is proportional to the applied field. These vortices can be thought of as circulating charge, where the center of the vortex is devoid of charge, which is all located on the edges. It is energetically beneficial for the electrons to pair with these vortices. It turns out that the number of vortices that pair with each electron determines whether or not a composite fermion or boson is formed. It is these composite particles that are then generating the FQHE. It turns out that it was the impurities in the original 2DEG that prevented the IQHE from being observed. Please note that this is vastly simplified if you want to know the full story I strongly recommend that you read Laughlin's Nobel lecture. My source for the QHE up to

this point has been Störmer's Nobel lecture which can be found at http://nobelprize.org/.

It turns out that graphene is ideal for the quantum Hall effect because it is perfectly two dimensional. Depending on applied electric fields it can also have positive and negative charge carriers which are Dirac fermions (i.e. their mass vanishes). As such, graphene exhibits a FQHE, but instead of the usual random fractions, only the $2h/e^2$ Hall resistance is measured[4]. Graphene is such an excellent material for this purpose that the QHE was observed at room temperature! This is astonishing because the QHE is normally associated with fractions of a Kelvin in order to minimize electron scattering. Figure 1.4 shows the data for the room temperature experiment. This is observable because the scattering of the effectively massless charge carrier remains small even at such high temperatures[5]. Before attaching the appropriate electrodes to the graphene many groups use standard processing techniques to shape the graphene into a Hall cross as depicted in figure 1.5[15].

(a) This is a graphene Hall cross on $300nm$ of SiO_2. Each terminal is connected to a gold electrode. This image is taken from Novoselov's paper on the room temperature observation of the quantum Hall effect[5]

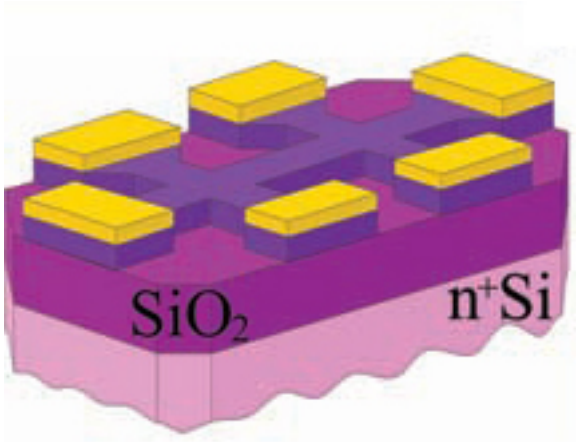

(b) This is a schematic of what a graphene Hall cross would look like when connected to gold electrodes and resting on top of SiO_2. This image is taken from Novoselov's paper on the electric field effect in graphene[3].

Figure 1.5: *An optical image and schematic of a graphene Hall cross connected to gold electrodes. The size of the Hall crosses are on the order of a few microns.*

1.2.3 Nano-ribbons: Optical and Electronic Effects

Before graphene was discovered carbon nano-tubes(CNTs) were an example of a reduced dimensional world. The single walled tubes (SWCNTs) with diameters below a nanometer are essentially one dimensional and also bestow their electrons with interesting properties. It turns out that SWCNTs can be metallic or semi-conducting depending on the orientation of the hexagons that make up the tube. If you consider a SWCNT to be a rolled up sheet of graphene, then there are many ways to create a cylinder so that the bonds seamlessly match up. Figure 1.6(a) shows the possible rolling vectors. If the correct vector is used the tube will be metallic; otherwise it will exhibit a band gap[16]. Interestingly, if pieces of graphene are somehow etched down to a width comparable to the SWCNTs, then they exhibit many of the the same properties, including band gaps and optical exciton spectra. The specific properties of SWCNTs will be discussed in a later chapter when we consider the importance of graphene alignment.

Figure 1.6(b) shows how the band gap in nanoribbons starts to become significant compared to random thermal excitations at room temperature as the width of the ribbon drops below $10nm$. Other predictions of confinement effects include interesting optical spectra[14]; careful alignment allowing for circuit elements such as resistors, capacitors, transistors, and splitters[7]; quantum dot transistors[17] and much, much more. People are constantly generating new calculations that predict wonderful and interesting properties for graphene, many of which we could test right here at Pomona if we develop the capability to finely shape the material.

1.3 Alternative Shaping Methods

We have recently acquired an extension to our scanning electron microscope (SEM) that allows us to perform e-beam lithography and with some optimization might also allow us to

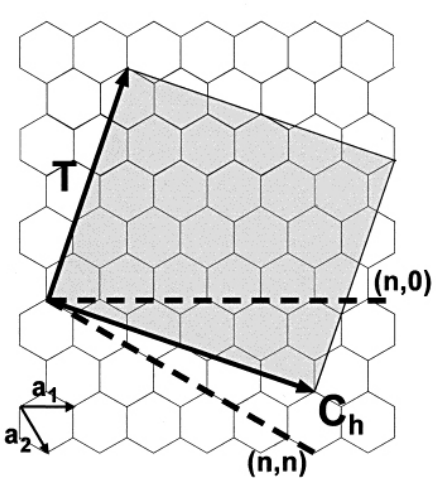

(a) This image is adapted from Odom's review of nano-tube structure[16]. The (n,n) and (n,0) vectors are called the armchair and zig-zag vectors because of the shape they cut out of the lattice.

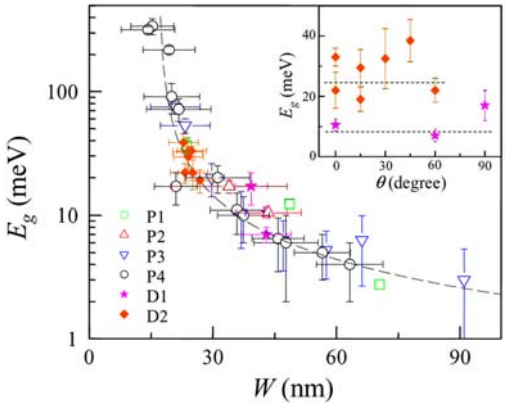

(b) This image is adapted from Han's paper on band-gap engineering in graphene nanoribbons[18]. The inlay examines the band gap as a function of the orietation of the crystal lattice.

Figure 1.6: *A schematic of the graphene lattice, and a graph of band-gap as a function of width for graphene nanoribbons.*

generate feature sizes down to $30nm$. We also have access to both negative and positive tone resist, so that with some optimization and experimentation we can generate useful masks. There are two sticking points in this process. First, because the graphene is randomly deposited, it will be tricky to locate it in the SEM so that a mask can be written on it without randomly exposing many places of the chip with the e-beam that are irrelevant and maybe even detrimental to the experiment.

The second problem we run into is with the Reactive Ion Etching (RIE). For various reasons including cost, safety, and high maintenance we do not own a machine that is designed for creating oxygen plasmas. Despite not having access to an oxygen plasma we have tried several methods that we thought would etch graphene in a controlled manner. One of the simplest possibilities to try was to burn it off. In Millikan there are a few chemical vapor deposition (CVD) furnaces that are capable of heating up to over $1000°C$. If we have O_2 running through the furnace while it is hot, or even just leave it open to the atmosphere, it

may be that the exposed graphene will combust. While this would almost certainly succeed if we were able to raise the temperature much higher, given the limitations of the material used for the mask this may not be viable.

A second method we examined was using ultraviolet lamps to generate ozone a highy reactive gas. There are several uv-lamps on campus, and in some instances they are designed to clean surfaces. We hoped that if our graphene samples were placed within a chamber full of uv-ozone, the gas would act analogously to the aforementioned oxygen plasmas.

A third technique we tested was to use a small plasma sputter-coater/cleaner located in Millikan, so that instead of generating a plasma in air, a DC Argon plasma would be formed. With the correct biasing of the sample this would cause heavy, non-reactive Argon ions to crash into the surface of the sample, physically sputtering away any feature that is left unprotected by a resist mask. While none of these methods turned out to be ideal, we did manage to get working results from two of them.

Chapter 2

Background Information

2.1 Previous Research

This project was not my first exposure to carbon related research. Over the course of two summers spent with the McEuen group at Cornell, and related research that I carried out here at Pomona, I have gained considerable experience in this field. I started out developing recipes for carbon nanotube growth, and later I moved onto fabricating and characterizing suspended few-layer graphene devices that were used as electromechanical resonators[6]. I also did some work where, instead of resonating the suspended graphite, I pushed down on the suspended sheets with an Atomic Force Microscope (AFM) tip in order to extract information about their physical properties[13]. These last two projects were published. Prints of these papers are in Appendix A and B. Because of my background in carbon related research I was interested to continue down this avenue for my thesis project.

2.2 Equipment

One of the factors in deciding to take on this project was the availability of many of the resources required to carry out any lithography or graphene deposition we might need. Although this equipment was not always in working order, fundamentally we had all the components we would need to deposit graphene, image and and characterize it, and then lithographically create an etch mask. The keys to these processes are in order: Pure flakes of graphite that we have previously used to make suspended few-layer graphene pieces, an optical microscope that we have previously calibrated to the color, and therefore the thickness, of the thin pieces of graphite, an Atomic Force Microscope allowing us to obtain detailed topographic maps of the fabricated devices, and finally a Scanning Electron Microscope equipped with a Nanometer Pattern Generation System (NPGS) that would allow us to easily generate masks at the micron scale using e-beam lithography. On top of these existing capabilities we also had three different potential methods for etching the graphite once the masks were in place, even if the most common method of an oxygen-plasma etch was not available.

Another tool that we did not anticipate using but turned out to be very useful was our maskless photolithography system that utilizes a modified DLP projector that can be used in conjunction with a computer to expose just about any pattern you could generate on screen. While it is simple to use and inexpensive it does have many limitations, mainly in its resolution. It is very difficult to expose any features under $20\mu m$ and therefore would be useless for the purposes of creating etch masks for our comparatively tiny pieces of graphene, but as a tool for creating the alignment markers in the SiO_2 substrate it turned out to be invaluable. In particular, because it is such a simple tool it is quite robust and reliable.

2.3 Lithography

2.3.1 Optical Lithography

Figure 2.1: *Our maskless lithography system. The projection lens of the DLP projector has been reversed and then mounted onto the microscope so that the image is projected into the focal plane of the microscope. Notice the amber overhead lights.*

Over the course of this project we made extensive use of both optical and electron-beam lithography. These are highly developed methods that are at the core of the semiconductor industry and a staple for any person who wishes to engage in nanoscale research. The fundamental idea behind the techniques is to focus some sort of chemically disruptive effect down to tiny areas so as to locally affect a surface. We then take advantage of this highly localized variation to produce features that are readily reproducible. Optical lithography has a huge advantage in that it has an extremely high throughput and is therefore used by the semiconductor industry to mass produce chips. Given the correct equipment one can expose the entire surface of a 12" wafer within a few minutes, while if one were to attempt to individually draw out the features it could take days or even weeks.

The key to the process is a polymer called "photoresist." This special polymer can be "spun" onto the surface of a substrate in an incredibly uniform manner. The photoresists, as implied by their name, are extremely sensitive to light. In particular they are often engineered so that they have high sensitivities to certain wavelengths. Historically these wavelengths have corresponded to the spectral lines of

mercury because mercury discharge lamps were an easy way to get uniform, intense light in an extremely narrow bandwidth. As such, most photoresists used are susceptible more energetic photons, usually in the UV. For this reason there will always be amber overhead lights in rooms where photolithography is carried out. These are specially filtered so that the photons illuminating the room have a minimal interaction with the resist.

When the resist is exposed to light of the correct wavelength a few different things can occur. The effects of the exposure depend on whether you have a negative or a positive tone resist. With a positive tone resist the photons break up the chains that form the polymer, often by releasing acid groups. While this has very little noticeable effect, when the sample is placed in a special developer the areas on the surface that have been altered by exposure to light will dissolve much more easily than the intact chains of the polymer surrounding them. This means that after exposure to the developer the areas of the resist that had been affected by the light will have disappeared, revealing the substrate beneath in exactly the pattern you tailored. You can now run any process that you wish on only the exposed areas, such as depositing metals, or etching away any exposed materials.

Negative tone resist, as suggested by its name, is the opposite of positive tone resist. Instead of removing the light-exposed pattern, the developer leaves behind the pattern while removing the rest of the polymer. There are a few different mechanisms for this but one way to think about it is that the light is so intense that it goes beyond breaking up the chains, and actually fuses them together, forming cross links. This means that these areas are actually harder to dissolve than the surrounding unaffected polymer, and after an appropriate development the exposed pattern remains behind as a mask.

While photolithography has been pushed to its natural limits by ingenious methods such as submerging the setup inside of a liquid with a higher index of refraction than air and taking advantage of induced phase differences in coherent light, the pitch of the pattern is fundamentally diffraction limited. That is while very smart tricks can be used to obtain

minuscule features it is very hard to have them repeat with a pitch smaller than $\lambda/2$. There are currently efforts to use Extreme Ultra Violet (EUV) radiation so as to minimize the wavelength, but if you want to make extremely small features you need change the paradigm and switch from photons to energetic electron or ions whose wavelengths, as determined by the De'Broigle relation, are tiny in comparison to even x-rays.

2.3.2 E-Beam Lithography

While e-beam lithography is somewhat of an art form, it is a very well established one. Research groups across the world use it in order to create features down to the nanometer scale. The idea is that the process of photolithography is duplicated but photons are replaced by energetic electrons. Instead of using a mask to determine which areas are exposed and which are not, a well focused electron beam, whose spot size can be less than a nanometer, is scanned over the resist in the desired pattern resulting in a change in the chemistry of the polymer. The sample can then be developed in the same manner as with a photoresist. Unlike photolithography the main mechanism for exposure is not the incident particles, but rather the much less energetic secondary electrons that are expelled by the collisions of the high energy e-beam with the surface of the sample. This means that while the beam is focused down to spot of a nanometer or less the actual minimum resolution that we can achieve is roughly $30nm$. This resolution can be lowered by varying the beam energy, and dedicated e-beam writers are able to go to line widths of under $10nm$. Like many e-beam writers in the world ours is not dedicated to this purpose. NPGS is an add-on to our Scanning Electron Microscope (SEM). While this means that the operating parameters of the instrument are not optimized for the purposes of beam writing, the reproducibility and resolution is still far better than what we could hope to achieve optically in our setup. There are several drawbacks to this method, so it is only used when the resolution required does not allow the use of optical methods. First of all it has a much lower throughput. The e-beam

needs to operate in a vacuum, so sample preparation becomes an issue. It also takes more time to expose features, particularly if you wanted cover the entire surface of a wafer with fine features. What might take optical systems a few minutes can take hours, or even be unfeasible due to the drift of the system over time. Therefore it is not used in a "production" mode but is an R&D tool. Another drawback is that you have to bombard your sample with electrons. This can be detrimental, particularly if you are attempting to build electronically sensitive devices.

2.4 Electronic Structure in a Honeycomb Lattice

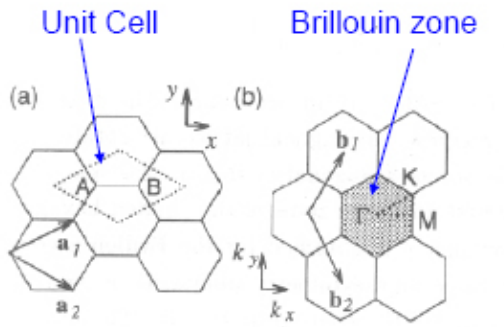

Figure 2.2: *Depictions of the honeycomb lattice and its reciprocal lattice in $\vec{k}$-space. As you can see the hexagonal symmetry is preserved, although the orientation is rotated. This image was taken from [19]*

The importance of the alignment of the crystal lattice of graphene has been known for years. Before graphene was the hot topic for carbon researchers there were nanotubes, and before that the Buckminsterfullerene (affectionately nicknamed the Buckyball). As previously discussed, single walled carbon nanotubes (SWCNTs) can be thought of as merely a rolled up sheet of graphene. The manner in which this rolling occurs determines the electronic properties of the nanotube. When rolled in certain way it is metallic, and in some other orientation it becomes a semiconductor. The physics behind this transition is well understood, and it will be beneficial to introduce some of the basic concepts here. While these effects do not matter in a large sheet of graphene that locally appears to be an infinite plane, in experiments where

the graphene is cut down to small dimensions that approach SWCNT diameters people have found that the orientation begins to matter. While the immediate future of this experiment will not require an implementation of this knowledge, any advanced experiments that we attempt will require a careful determination of the lattice orientation of any graphene sheet we attempt to use. This will require the use of scanning tunneling microscopy (STM) which can be carried out here on campus.

2.4.1 The Band Structure of Graphene

Even though graphene is a better conductor than just about any other material, it is not in fact a metal: it is a zero band gap semiconductor. This means that the valence and conducting bands are degenerate at the fermi level but they do not actually overlap, which means in turn that electrons in the lattice are not allowed to occupy such a state. In bulk graphite the interlayer interactions cause the two bands to overlap making it a metal; however these interactions are impossible in an isolated 2-D sheet. In order to understand the electronic properties it is necessary to think not in position space, but in momentum space. The representation of the electrons in the honeycomb lattice retains a hexagonal symmetry when we look at the "reciprocal" lattice in momentum space. The individual hexagons in the reciprocal lattice form what are called Brillouin Zones (See figure 2.2). Because of the periodic structure of the material a large portion of the electronic structure can be described simply by examining the first Brillouin zone.

Using what is called the tight binding method one can actually calculate the dispersion relation for graphene, that is, the relationship between the electron energies and wave-vectors (related to the momentum and represented as $\vec{k}$). Equation 2.1[19] gives the result of this calculation, and figure 2.3(a) is a wireframe representation of the resulting equation. In equation 2.1, a is a constant related to the dimension of the graphene lattice while t is the result of what is called the transfer integral. The points where the π and π^* bond meet are

labeled as the K points. This is where there is a degeneracy between the two states and is the fermi energy, i.e. the energy level that the electrons fill up to at $T = 0$. Because the density of states is zero at these points, graphene is not a metal; it is a semiconductor which happens to have a zero band gap.

$$E(\vec{k}_x, \vec{k}_y) = \pm t \left[1 + 4\cos\left(\frac{\sqrt{3}\vec{k}_x a}{2}\right)\cos\left(\frac{\vec{k}_y a}{2}\right) + 4\cos^2\left(\frac{\vec{k}_y a}{2}\right)\right]^{\frac{1}{2}} \tag{2.1}$$

2.4.2 Transitioning to 1-D

Because of the large numbers of symmetries of the structure of graphene, if we attempt to roll a sheet into a nano-tube there are many possibilities for the bonds to match up and allow for a seamless transition to an infinite cylinder. The specific manner in which a nanotube has been rolled is characterized by the chirality vector ($\vec{C}_h$). As you can see in figure 2.3(b), $\vec{C}_h$ is a linear combination of the unit vectors of the honeycomb lattice ($\vec{a}_1, \vec{a}_2$. When the tube is rolled $\vec{C}_h$ becomes the circumference, and $\vec{T}$, the vector perpendicular to it, follows the length of the tube. It turns out that the band structure of a tube is entirely determined by its chirality, which can be thought of as a measure of how "twisted" the tube is.

The unit vectors of the lattice are known as "zig-zag" (a_1 or a_2), and "arm chair" (a_1 and a_2) If in figure 2.3(b) you follow the vectors $\vec{a}_1$ and $\vec{a}_2$ in the correct manner, they will trace out a zig-zag and an armchair pattern respectively. From here on out we will label $\vec{C}_h$ by (m, n), where m, n are integers with $m \leq n$, and they are the scalars that multiply the unit vectors to form the linear combination that determines the circumference of a rolled up tube. A $(0, n)$ tube is one extreme and is called a zigzag tube, while (n, n) is the other extreme condition which is the armchair tube.

If you consider that when the sheet of graphene is rolled up the boundary conditions change considerably it should not be surprising that we begin to see quantized behavior. Our boundary conditions require that any electron wave function should be periodic as we

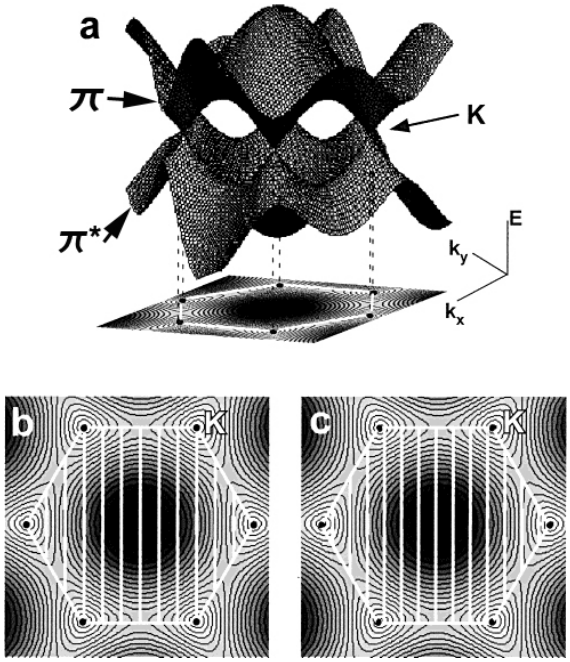

(a) A 3-D wire map of equation 2.1. The dark areas are the allowed energies for the electrons. Below the 3-D graph are two possible results of the quantization of the bands by rolling the graphene into a nanotube. One of the 2-D images has the white cuts crossing K-points the result: a metallic nanotube. This image was adapted from [16]

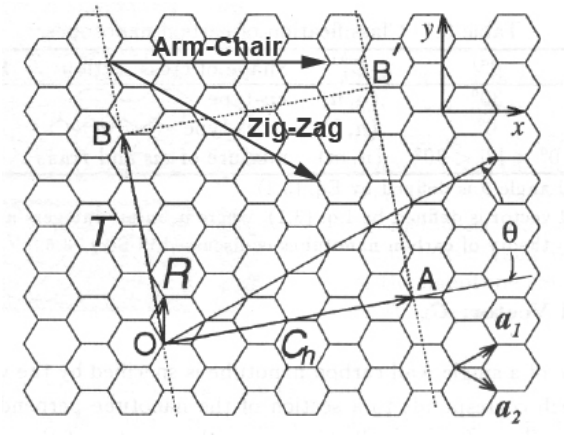

(b) A nice graphical representation of what the $\vec{T}$ and $\vec{C}_h$ physically represent in the honeycomb lattice. This image was adapted from [19]

Figure 2.3: *Figures relating to the physical and electronic structure of nanotubes and nanoribbons.*

travel around the circumference of the tube. That is being "single valued" requires that as we rotate the tube through 2π radians the wave function should match up with itself. This leads to N distinct allowed 1D bands , where N is the number of graphene unit cells contained in the nanotube unit cell swept out by $\vec{T}$ and $\vec{C}_h$. These 1-D bands are simply crossections of the graphene dispersion relation in figure 2.3(a). If these 1D cuts happen to pass through the K-Points of the graphene relation then the obtained tubes are metallic, and otherwise they have a band gap determined by the energy difference between the π and π^* bonds at that point. Figure 2.3(a)(b and c) shows two examples of such 1D cuts through the Brillouin zone of graphene. It turns out that if $n - m$ is an integer multiple of three then the conditions for a metal tube are met. This implies that 1/3 of all tubes

should be metallic. Another result is that the size of the bandgap in semiconductor tubes is inversely proportional to the diameter. Because the bandgap is determined by the energy difference between the π bonds at the point of the 1-D cut, having an allowed state closer to the K-points will result in a lower band gap. Because the number of 1-D cuts depends on the number of graphene unit cells contained in the unit cell of the tube, the larger diameter tubes will have more allowed states and therefore more states closer to the K points resulting in a lower band gap.

2.4.3 Unrolling a Nanotube

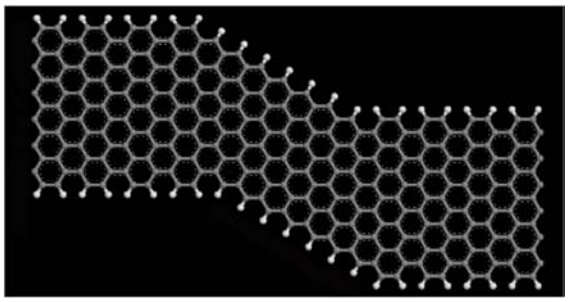

Figure 2.4: *A model of what graphene cut at different angles in order to induce metallic or semiconducting properties might look like. The two horizontal sections would be metallic while the center, diagonal section is designed to have a bandgap; effectively creating a transistor. This image was adapted from [17]*

Instead of rolling up a sheet of graphene into a tube, consider cutting it down into strips with widths comparable to the diameters of the tubes. Even though this setup does not have the same boundary conditions as that of a nanotube, it amazingly still retains many similar properties. Depending on whether the edges follow the zig-zag or armchair vectors we experimentally observe that the sections of the graphene are metallic or semiconducting, and the bandgaps of the semiconductor sections continue to vary inversely with the width of the ribbon. Because the periodicity of the bonds are broken at the edges, the way that the bonds are terminated becomes important. If they are hydrogen terminated then everything behaves well; however "dangling" bonds can cause problems. They are not "complete" and therefore cause scattering and charge trapping. Almost all nu-

merical models of graphene transistors and the therefore assume that the edges are hydrogen terminated.

This means that if in the future we attempt such experiments we will have to use Scanning Tunneling Microscopy (STM) in order to accurately determine the lattice orientations of our samples. We would also have to take measures to ensure that the edge effects are minimized by facilitating hydrogen termination of the dangling bonds.

Chapter 3

Experimental Procedure

3.1 Preparing the Substrate

There are certain oxide thicknesses corresponding to the illumination wavelength that maximize the visibility of graphene[2]. We had previously been using $280nm$ of oxide, however we switched to $100nm$, which gives the oxide a different hue; however, the thin pieces of graphite are still visible with white-light illumination. The advantage of the $100nm$ oxide is cost, as it is easy to commercially obtain these wafers, where as the $280nm$ oxide is more of a customized thickness that is only convenient if you have the furnaces required to grow your own thermal oxide or are prepared to pay for a customized batch of wafers. Our next step was to create patterns on the surface of the substrate that would allow us to locate any thin pieces of graphite that were deposited near them. This is a method of indexing that is analogous to the way that parking lots at stadiums and amusement parks are broken up into labeled (e.g. 1A) sections so as to be able to find your car in the sea of vehicles. We accomplished this using our maskless lithography system previously developed by former Pomona student David Musgraves [20]. Using the optical lithography we exposed a pattern in Shipley 1813 resist. The resist was "spun" on at $4000rpm$ for $45sec$ and had a thickness of

roughly $1.3\mu m$. Prior to spinning the resist the surface of the wafer was primed by spinning on organisilane which improves the adhesion of the resist to the surface. The exposure was carried out using the $5x$ microscope objective, and the timing of the exposure was controlled through the use of a Microsoft PowerPoint© presentation. The vertical and horizontal lines are $1pt$ thick and were exposed for $65s$, while the dots are $27pt$ and were exposed for $75s$.

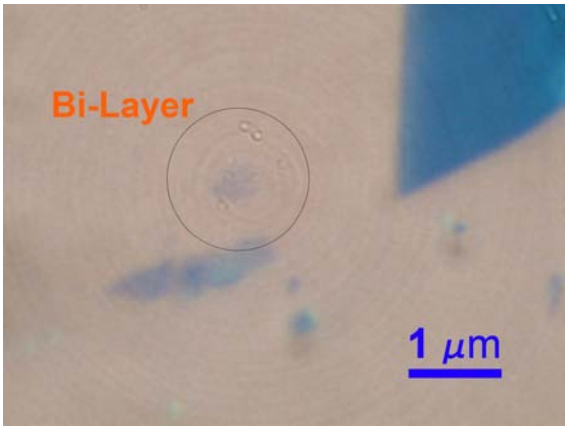

Figure 3.1: *An extremely thin piece of graphite on 100nm of oxide. The circled piece is* $1nm$ *thick as measure by Tapping Mode AFM and is still visible.*

After a chemical developing step in which the sample was dipped in Tetramethylammonium hydroxide (TMAH) for 90 seconds, the exposed polymer was washed away, leaving the oxide under the pattern exposed, as can be seen in figure 3.2(a). We then used 6:1 Buffered Oxide Etch (BOE) to etch away the exposed oxide. BOE is 49% Hydrofluoric acid that is buffered with Ammonium Fluoride[21]. Since the HF by itself would attack not only the SiO_2 but also the photoresist, the ammonium in the buffered solution protects the photoresist while leaving the oxide susceptible to the fluorine ions, allowing for extremely selective etches of the SiO_2. After removing the remaining photoresist we were left with $100\mu m$ scale patterns that could be used for alignment and location in the SEM and the AFM. Figure 3.2(b) is an example of an array of boxes that will be easily identifiable because of the patterns of dots inside and out of the boxes. The dots were specially designed so that an inverting microscope would not confuse the issue.

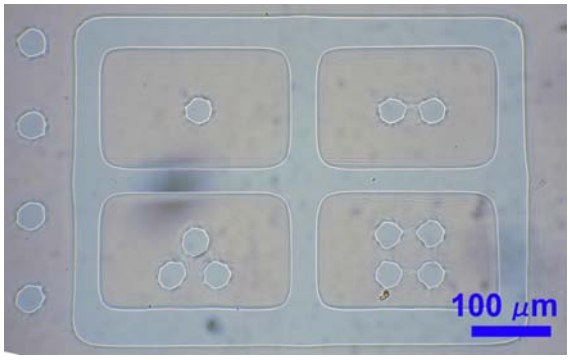

(a) One of our alignment markers that has been exposed and developed. At this point the oxide is still intact and the pattern is only in the photoresist.

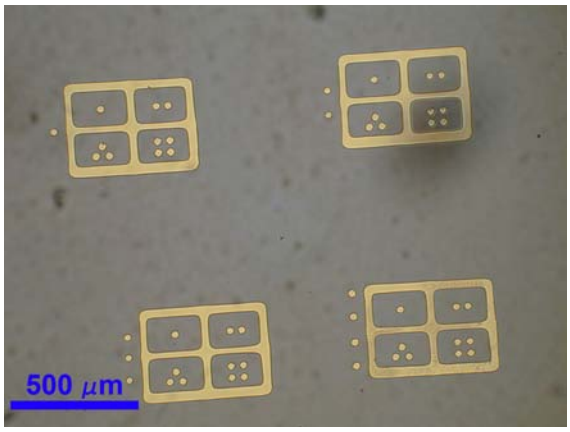

(b) This is a group of 4 alignment markers. You can see that the patterns of the dots will allow for finding a piece of graphene near these marks while avoiding issues with inverted images. The purple/gray hue of the SiO_2 is characteristic of 100nm of thickness.

Figure 3.2: *2 stages of the optical lithography and etching process that results in our alignment marks.*

3.2 Depositing Graphene: The Miracle of Scotch Tape

The method for actually depositing graphene is so rudimentary as to be amusing. The trick is finding the thin flakes of it after deposition. Very simply: we take a $6in$ long piece of scotch tape, place a flake of Kish graphite (see figure 3.3(a)) on it and fold the tape over the graphite multiple times until the entire surface is coated with very thin flakes of graphite. An example of such a piece of tape can be seen in figure 3.3(b). A suitably homogeneous section of the tape surface is then pressed onto the SiO_2 substrate and the back side is rubbed with tweezers, or a pen; anything to apply localized pressure. This then transfers some of the graphite flakes, hopefully very thin ones, to the surface of the substrate. The graphene is very effectively stuck to the surface due to the van der Waals interaction, which due to the size scales and relatively large surface area to mass ratios involved is dominant over other forces that might displace the sheets.

Subsequent examination with an optical microscope, and the incredible image processing

power of the human brain, then allows us to locate the very thin pieces. We can then use AFM to determine the actual thickness down to the the level of a bi-layer, however, once your eyes become calibrated the step with the AFM starts to lose its significance. In order to find the sample in the AFM it is very useful to have the alignment marks we etched into the oxide; otherwise, finding a sample that was found in a dedicated optical microscope is virtually impossible.

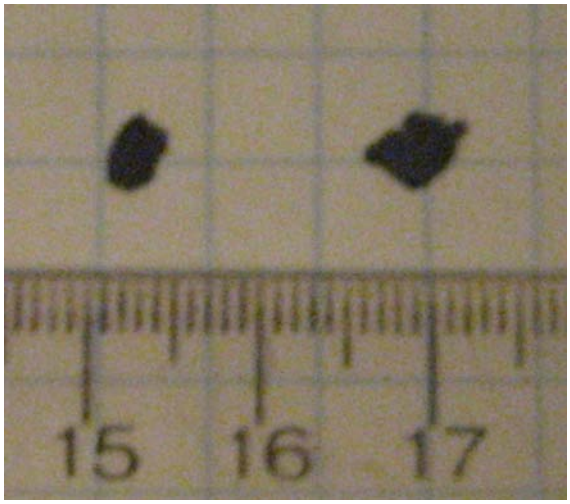

(a) Two flakes of kish graphite next to a ruler.

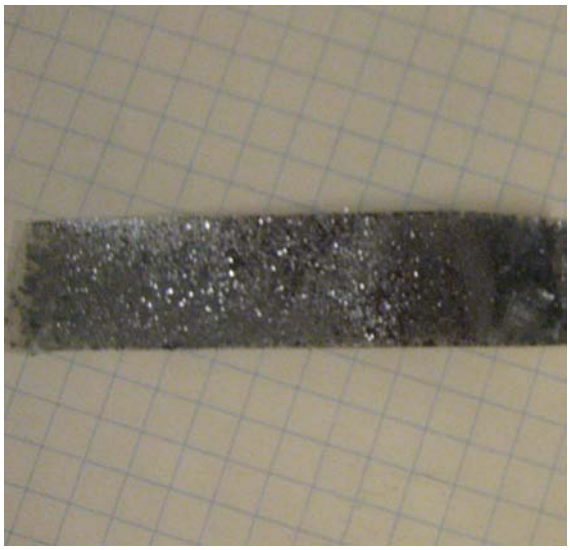

(b) A piece of standard scotch tape that has been almost completely covered by flakes of graphite after repeated folding.

Figure 3.3: *The mysteries of Kish graphite revealed.*

In order to determine if an extremely thin piece of graphite is in a fact a single atomic layer, i.e. graphene, there are some techniques required that we do not have access to here. One would assume that given the topographic sensitivity of an AFM you would simply be able to determine the thickness of one layer, measure any sample you have and divide by the thickness of a single layer to get the number of stacked sheets. Unfortunately this method does not work for few-layer graphene sheets. The predicted thickness of a single layer is 3Å; however, due to the different tip surface interaction while the tip is over the graphene or the oxide you can never measure a step height lower than about 9Å. This means that in order

to get a definitive reading on whether you have 1 or 2 layers of graphene, either Raman Spectroscopy or observation of the Quantum Hall effect is required[22, 23, 24].

One drawback of this method of exfoliation is that it leaves behind large amounts of tape residue. This residue is inert; however, it does clutter the surface of the substrate and may conceal good samples as well as making AFM difficult. Therefore after deposition we have found that it is good practice to heat up the sample to $450°C$ in a furnace open to the atmosphere in order burn of all the tape residue, while leaving the graphite on the surface unaffected. This makes searching for and characterizing suitable samples much easier.

3.3 E-Beam Lithography

Once we have located a suitable piece of graphene or few-layer graphene piece, our next step is to create an etch mask for it. To this point the steps have been fairly rudimentary, however this next step requires sub-micron alignment because while writing the pattern with the electron beam in the SEM we will be "blind." The reason for this is that when the sample has been coated with our resist, in this case a spin-on glass, if we attempt to image it with the electron beam we will simply expose the resist. Therefore before we coat the sample with resist we need to take an image of it in relation to the alignment markers we created in the first step of our process. NPGS will then allow us to import this image into AutoCad and label parts of the image as alignment markers.

The resist that we used was Hydrogen-Silsesquoxane (HSQ), a spin on glass. This is a negative tone resist, so in contrast to our optical lithography the exposed areas will remain after development while the unexposed areas are washed away. This effect is due to the fact that the exposed glass polymer strands get cross linked. This allows for the unexposed areas to be dissolved much more easily by the developer. Once the sample has been coated with HSQ we can carefully approach the alignment marks with electron beam. Once NPGS has

found these alignment makers it can then appropriately move the stage or just the beam to write the pattern in the precise position and orientation that we want. As a demonstration of our capability we would like to write a simple hall cross which is a common application as well as a fairly simple pattern. Because NPGS is designed to be able to write $30nm$ line widths we should be able to very easily write a micron scale pattern on our graphene layers. Once the exposure has been completed we will then develop the chip in TMAH. After this step we should be ready to somehow etch the pieces of graphite not protected by our HSQ mask.

The following chapter deals with the various methods we attempted for etching. Unfortunately due to technical difficulties with the SEMs automated stage we are at this point unable to complete this portion of the experiment. Fortunately, due to the independent nature of the processes, we were able to characterize various methods for etching the graphene. Figure 3.4 is a graphical representation of the various steps with the lithography and etching and how our final sample will emerge.

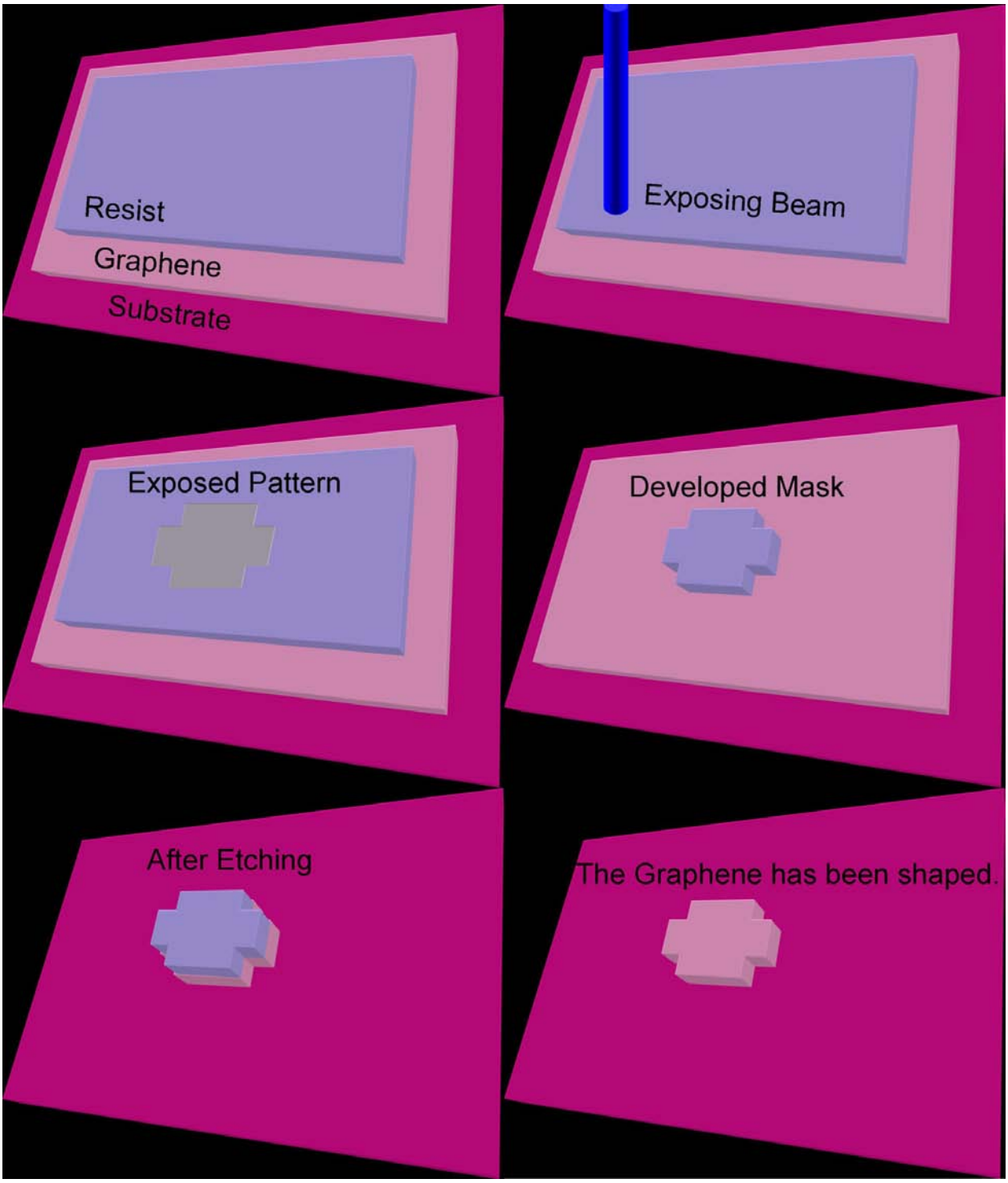

Figure 3.4: *A graphical representation of the various stages of lithography and processing.*

Chapter 4

Methods for Removing Graphene

4.1 UV Ozone Etching

One of the methods we attempted to use that would remove any exposed graphite was Ultra-Violet Ozone Etching. The idea behind this method is that very high energy photons that collide with the oxygen in the atmosphere cause some of the O_2 molecules in the air to form O_3, which is highly reactive. If there is a high enough density of ozone we would expect that it would react with any exposed carbon to form CO_2. Unfortunately for the intensity of lamps we had available, including a commercial UV ozone cleaner, were unable to make a visible impact on graphene samples, even after tens of

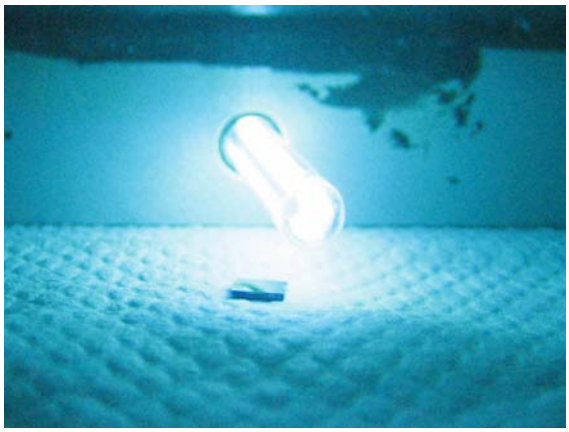

Figure 4.1: *An image of a small UV-Penlamp taken while it is on. Obviously the wavelengths that generate the ozone are not visible, but the emitted spectrum extends into the violets. These lamps should never be viewed with the naked eye.*

minutes of exposure. We therefore abandoned this idea, particularly as we were receiving much more promising results from the other methods that we were pursuing.

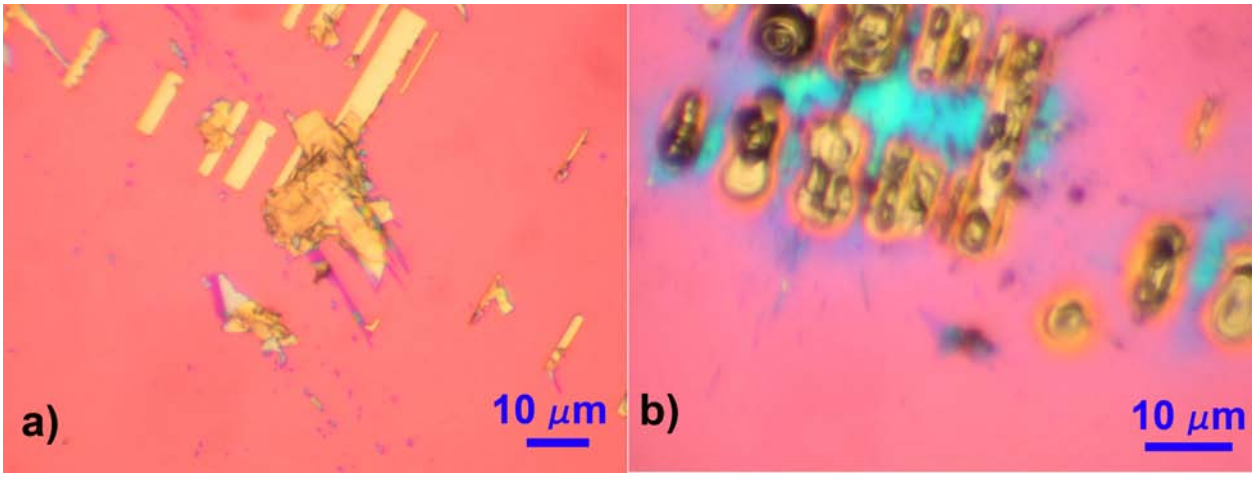

Figure 4.2: *(a) An optical micrograph of an SiO_2 substrate with graphite of various thicknesses on the surface. The thinner pieces are characterized by their purple color. The white rectangles are trenches that have been etched down to the silicon below the oxide. (b) This image is of the same area as part (a) after it has been sputtered by a DC Argon plasma for 5 minutes. The thinner pieces of graphite have disappeared and considerable amount of violent damage has occured.*

4.2 Argon Sputtering

One of the easiest methods of etching the thin graphite layers was through the use of a DC Argon Plasma. We are able to generate an Argon plasma where an Oxygen plasma would be impossible because Argon is inert and therefore does not require any special vacuum pumps or safety precautions. Using our Hummer II Sputter Coater/Etcher we were able to create DC Argon plasmas that very effectively removed graphite on the surface of an SiO_2 chip. In figure 4.2 we show a selected sample of very thin graphite pieces, less than $5nm$ in places, that have been etched by the argon plasma. While this method does remove the exposed graphene layers it also has some deficiencies in that it is very violent, and in many places the substrate's surface oxide has been cratered and destroyed by arcing. It also slowly etches

away the underlying substrate. While this is much slower than the rate at which carbon material disappears, it can still become an issue, particularly in that material under a sheet of graphite is shielded and thus ends slightly raised above the remainder of the substrate.

Typically the etches were carried out at an Argon pressure of $100mTorr$, with the high voltage adjusted so that the ion current was $10 - 15mA$. It is impossible to give an accurate number for what this voltage is because the dial is not calibrated but simply shows arbitrary units. If the voltage is raised much higher, then the arcing on the chip becomes a considerable factor. At this etch rate it typically takes $3 - 5min$ for the thinner pieces of graphite to disappear. This number is not exact, and it does not appear that the surface is uniformly etched, so some pieces of similar thicknesses will survive while other thin sheets of graphite are etched. If the etching continues for too long the oxide substrate becomes degraded, and its thickness can be changed significantly enough that then thin pieces of graphite on its surface start to lose their contrast. Therefore it is inadvisable to etch for more than 10 minutes, so this is not a viable option to remove thicker pieces of graphite. As can be seen from the color of the oxide in figure 4.2, the thickness of the tested oxide was $280nm$. However, we have subsequently switched to oxide thicknesses of $100nm$, which could be a problem if the thinner oxide results in greatly increased arcing, because the thinner layer will breakdown more easily due to the voltage buildup between ions on the surface and the silicon that the oxide covers.

This method does, however, have the advantage being extremely quick, and easily controlled. The Hummer is able to pump down to its operating pressure in a matter of minutes, and we can then precisely control the flux of ions to the surface of the sample, and thus the rate at which we expect material to be etched away. All in all it takes roughly 10-15 minutes to perform a run.

4.3 High Temperature Furnace

The method of placing the graphene inside a high temperature furnace also yielded some promising results. As can be seen in figure 4.5 almost all of the carbon on the surface of the substrate was removed while the SiO_2 remained relatively unharmed. Some of the exposed silicon in the trenches was discolored, however, compared to the effects of the argon etch it seems benign. We are still in the early stages of testing this technique so we may yet get better results, although there are many drawbacks. First of all these furnaces are extremely slow to operate. They take tens of minutes to heat up to their operating temperatures, and then they take about an hour to cool back down once the run is complete. This makes for not only time consuming operations but also difficulty in controlling the exact amount of heat that the graphene will be exposed to. Currently we are simply leaving the furnace open to the atmosphere for an hour at $1000°C$, and the process completely removes any traces of graphene from the surface. However, we may be able to vary this time scale, and more precisely control the temperature exposure, by sliding the sample into and out of the furnace while the furnace is hot. Another possibility is that instead of heating the sample in the ambient atmosphere we were to flow pure oxygen over it. This would almost certainly allow us to operate at lower temperatures, meaning there

Figure 4.3: *The Hummer II DC Plasma Etcher that we used. The purple color of the plasma in the chamber at the top of the machine is characteristic of Argon.*

would be less stress placed on any mask we would choose to use, as well as faster operating times.

Figure 4.4: *This furnace is normally used in the growth of nanotubes. It is capable of reaching over* $1100°C$*, which is well above the temperature at which the graphite we use combusts.*

In order to be able to use this to not just remove all graphite from the surface, but to only remove the exposed areas of a sheet of graphene we have to find a suitable material for the mask. A possible candidate for the high temperature masks is hydrogen silsesquioxane (HSQ), which is a negative tone e-beam resist, that can maintain its shape at over $1000°C$, meaning that it can easily withstand the temperatures at which we observe the graphite burn.

However, this material has its own drawbacks. After it is baked in the furnace it will essentially become glass. While removing glass is not very difficult, our problem arises from the SiO_2 that the graphene needs to be on top of to be visible. Since this material is also essentially glass and any chemical that etches the HSQ will also etch SiO_2. If this etching is isotropic, as most wet-etches are, then the areas covered by the mask will be undercut, and if the features narrower than the thickness of the resist they will be cut off and float away in the etchant. This will not however be a problem in with the feature sizes and resist thicknesses we plan to operate at.

Another unknown is whether such a mask actually will protect the graphene below it. In the case of the argon etching the effect is top down, and any layer covering the graphite will prevent it from being attacked. However, in a furnace operating at several hundred $°C$ we do not know if the graphene under the mask will not simply burn away along with the

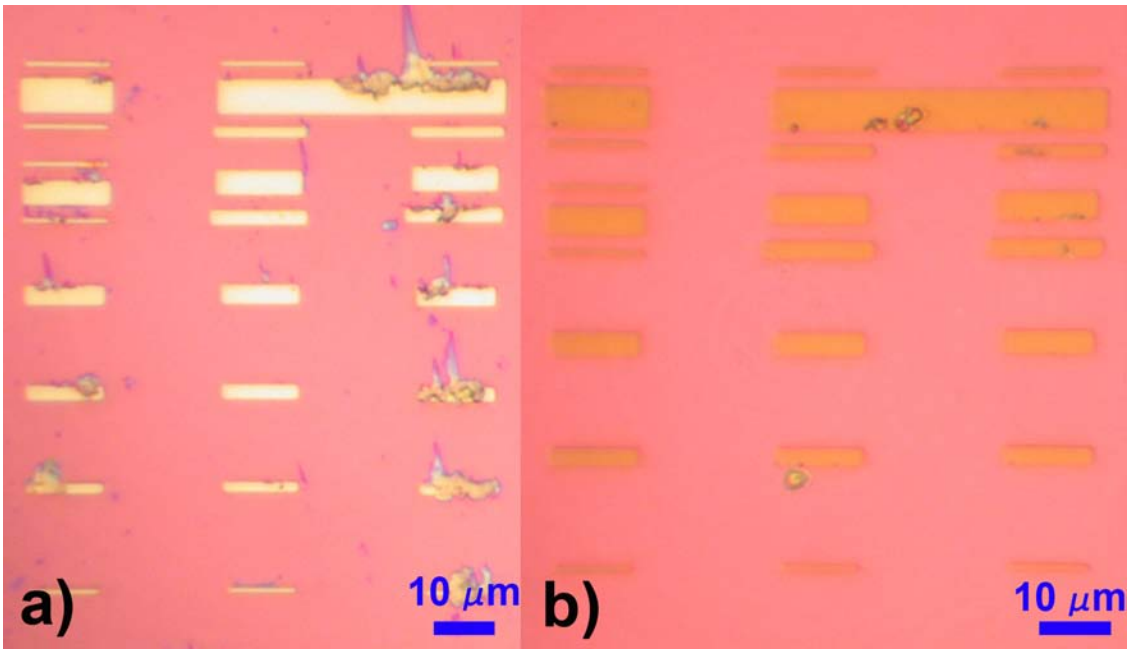

Figure 4.5: *(a) Some trenches in SiO_2 with graphite of varying thicknesses. (b) The graphene has been burned off at* $1000°C$*. Notice that only some glue residue is left behind.*

exposed areas. Logically the aspect rations involved and the difficulty any oxygen would have in reaching under the mask to burn the carbon seem fairly negligible. Unfortunately we will not know if this will be an issue or not until after we test the process, when our e-beam capabilities are in order.

Chapter 5

Conclusions

Despite many promising results we have not yet been able to attain our final goal of creating a Hall cross from graphene in order to demonstrate our capability of shaping graphene. We have however found that we could remove any exposed graphene, and even larger pieces of graphite, by either a DC Argon plasma or a high temperature furnace run. We have also modified SiO_2 substrates so that they are equipped with alignment markers that allow us to find the pieces of graphene we mechanically exfoliate in both the AFM and SEM. Therefore, once the SEM stage is fixed we should be able to expose a micron scale mask on our graphene samples through the use of the excellent NPGS alignment system. We could then test how our various methods for removing graphene are compatible with the HSQ masks we plan to use.

We are extremely confident that the e-beam lithography step will work. This is because it is a well established technique. In comparison we really *do* need to test if burning the samples in the furnace will be a viable method for shaping graphene. We definitely know that the high temperatures effectively remove all graphene, but we simply cannot know a priori whether or not the HSQ will protect and preserve the parts of the graphene under the mask. However, even if this method is unsuccessful we have shown that the argon plasma

will also remove exposed graphite, and because of the "top down" nature of the process this method will almost certainly leave behind a shaped piece of graphite.

Overall we have taken many positive steps towards developing a complete process for the shaping of mechanically exfoliated graphene. We have developed an alignment system which will allow us to carry out the e-beam lithography with precision placement. We have also demonstrated two different methods for removing graphene from the surface of a substrate, and we are extremely confident that once some preliminary technical issue are resolved we will be able to quickly complete any necessary e-beam lithography. All that remains to be tested is whether or not an HSQ mask will act as desired and protect a defined piece of graphene, and then finally we will need to remove the HSQ mask after the exposed graphene has been etched away. This final step should not be too difficult but will require some testing and experimentation.

Chapter 6

Acknowledgements

6.1 Pomona College

First and foremost I would like to thank David Tanenbaum for his advice and friendship over these last three years at Pomona. He was always been willing to support me in the projects I chose to pursue, and it has been a pleasure to work with him both in the lab and in the classroom where he is wonderful and dedicated teacher.

I would also like to thank Connie Wilson, David Haley, Glenn Flohr, and Michael Guerre: the wonderful staff of the Physics department who are always willing to help students. In particular David Haley and Glenn Flohr have been incredibly supportive and helpful in the laboratory environment and a pleasure to interact with on a personal level.

Although I have not known him for very long I would like to extend a special thank you to Ben Pollard, whose help was very much appreciated in doing an excellent job of developing the photolithography recipes for the alignment markers. Additionally Scott Berkeley was very helpful in teaching me the "scotch tape" method of depositing graphene which I had not previously used.

Finally the entire Physics faculty and my fellow Physics majors who have worked together

to make Millikan my favorite place to hangout. Particularly I would like to thank Alex Baum, Bryant Forseman, Erica Nelson, Gordon Stecklein, and Lua Del Campo: my fellow seniors. They were there throughout all the hundreds of problem sets and suffered through my incessant presentations about graphene and nanotechnology.

6.2 Cornell University

Some of my fondest memories from the last four years are the two summers I spent at Cornell working in the McEuen group. Prof. Paul McEuen was extremely generous in allowing me to spend 10 weeks each summer working in his labs. The entire group was also incredibly friendly and helpful to a young undergraduate learning the basics of doing advanced research. In particular my mentor Arend van der Zande was an amazing teacher and a friend. Along with David Tanenbaum he is one of the people who helped me discover the beauty and joy of research, and inspired me to go on to graduate school in Physics.

Appendices

Appendix A

Electromechanical Resonators from Graphene Sheets.

small bending and then must break, whereas columns with an aspect ratio of 80 can fully bend to touch the surface without breaking. An aspect ratio of at least 20 is needed for sufficient bending of each beam to touch its neighbors to obtain the structure shown in Fig. 4, C and D. This mechanical assessment makes it possible to design a hydrogel/nanocolumns combination that enables a desired degree of directed actuation.

We have developed hybrid architectures in which arrays of high–aspect-ratio silicon nanocolumns, either attached or free-standing, are embedded into a hydrogel film and are actuated into highly controlled, complex microstructures upon contraction and/or swelling of the polymer. The actuation is fast, reversible, reproducible, and robust. We believe that these architectures may lead to a variety of applications, including actuators, controlled reversible-pattern formation, microfluidics, reversible switching of the wetting behavior, tunable photonic structures, artificial muscles, and release systems (*25*).

References and Notes

1. S. Minko, *Responsive Polymer Materials: Design and Applications* (Blackwell, Ames, IA, 2006) and references therein.
2. Y. Osada, H. Okuzaki, H. Hori, *Nature* **355**, 242 (1992).
3. Y. Osada, A. Matsuda, *Nature* **376**, 219 (1995).
4. D. J. Beebe *et al.*, *Nature* **404**, 588 (2000).
5. T. P. Russell, *Science* **297**, 964 (2002).
6. J. Lahann *et al.*, *Science* **299**, 371 (2003).
7. A. Lendlein, H. Y. Jiang, O. Junger, R. Langer, *Nature* **434**, 879 (2005).
8. F. Chiellini *et al.*, *Macromol. Rapid Commun.* **22**, 1284 (2001).
9. M. Mayer, J. Yang, I. Gitlin, D. H. Gracias, G. M. Whitesides, *Proteomics* **4**, 2366 (2004).
10. T. Sun, L. Feng, X. Gao, L. Jiang, *Acc. Chem. Res.* **38**, 644 (2005) and references therein.
11. K. Autum *et al.*, *Proc. Natl. Acad. Sci. U.S.A.* **99**, 12252 (2002) and references therein.
12. P. Vukusic, J. R. Sambles, *Nature* **424**, 852 (2003) and references therein.
13. A. K. Geim *et al.*, *Nat. Mater.* **2**, 461 (2003).
14. S. B. Lee, R. Koepsel, D. B. Stolz, H. E. Warriner, A. J. Russell, *J. Am. Chem. Soc.* **126**, 13400 (2004).
15. E. Delamarche, H. Schmid, B. Michel, H. Biebuyck, *Adv. Mater.* **9**, 741 (1997).
16. T. N. Krupenkin, J. A. Taylor, T. M. Schneider, S. Yang, *Langmuir* **20**, 3824 (2004).
17. L. Zhai, F. C. Cebeci, R. E. Cohen, M. F. Rubner, *Nano Lett.* **4**, 1349 (2004).
18. S. A. Asher, in *Nanoparticles: Building Blocks for Nanotechnology*, V. M. Rotello, Ed. (Kluwer, New York, 2004), pp. 145–172.
19. M. K. Maurer, I. K. Lednev, S. A. Asher, *Adv. Funct. Mater.* **15**, 1401 (2005).
20. S. Park, J.-H. Lim, S.-W. Chung, C. A. Mirkin, *Science* **303**, 348 (2004).
21. Materials and methods are available as supporting material on *Science* Online.
22. K. S. Iyer, B. Zdyrko, H. Malz, J. Pionteck, I. Luzinov, *Macromolecules* **36**, 6519 (2003).
23. B. D. Gates *et al.*, *Angew. Chem. Int. Ed.* **43**, 2780 (2004).
24. E. E. Ruppert, R. S. Fox, R. B. Barnes, *Invertebrate Zoology* (Brooks Cole Thomson, Belmont, CA, ed. 7, 2004).
25. In particular, our preliminary data show that these structures (i) direct the flow and particle transport (analogous to the function of cilia in organisms) and thus have potential in microfluidics, (ii) reversibly change their photonic properties and thus can be considered for tunable photonics, (iii) reversibly switch their wetting behavior from superhydrophobic in the humid environment to hydrophilic in the dry environment, and (iv) trap and release particles in microflowers.
26. R. Buckminster-Fuller, *Portfolio Art News Annu.* **4**, 112 (1961). Also available at www.rwgrayprojects.com/rbfnotes/fpapers/tensegrity/tenseg01.html.
27. D. E. Ingber, *Annu. Rev. Physiol.* **59**, 575 (1997).
28. M. Defossez, *Mech. Res. Comm.* **30**, 311 (2003).

29. We thank P. Kolodner, J. Weaver, I. Luzinov, and I. Sokolov for fruitful discussions. We thank R. Smith and N. Lippa for technical assistance. This work was supported in part by the Office of Naval Research, award N00014-05-1-0909.

Supporting Online Material

www.sciencemag.org/cgi/content/full/315/5811/487/DC1
Materials and Methods
Figs. S1 to S5
Table S1
References
Movies S1 and S2

25 September 2006; accepted 7 December 2006
10.1126/science.1135516

Electromechanical Resonators from Graphene Sheets

J. Scott Bunch,[1] Arend M. van der Zande,[1] Scott S. Verbridge,[1] Ian W. Frank,[2] David M. Tanenbaum,[2] Jeevak M. Parpia,[1] Harold G. Craighead,[1] Paul L. McEuen[1]*

Nanoelectromechanical systems were fabricated from single- and multilayer graphene sheets by mechanically exfoliating thin sheets from graphite over trenches in silicon oxide. Vibrations with fundamental resonant frequencies in the megahertz range are actuated either optically or electrically and detected optically by interferometry. We demonstrate room-temperature charge sensitivities down to 8×10^{-4} electrons per root hertz. The thinnest resonator consists of a single suspended layer of atoms and represents the ultimate limit of two-dimensional nanoelectromechanical systems.

The miniaturization of electromechanical devices promises to be as revolutionary in the coming decades as the miniaturization of electronic devices was in the previous ones. Devices ranging from nanoscale resonators, switches, and valves have applications in tasks as diverse as information processing, molecular manipulation, and sensing. The prototypical nanoelectromechanical system (NEMS) is a nanoscale resonator, a beam of material that vibrates in response to an applied external force (*1*, *2*). The ultimate limit would be a resonator one atom thick, but this puts severe constraints on the material. As a single layer of atoms, it should be robust, stiff, and stable.

Graphite consists of stacked layers of graphene sheets separated by 0.3 nm and held together by weak van der Waals forces (*3*). It has extremely high strength, stiffness, and thermal conductivity along the basal plane. In addition, graphite can be exfoliated onto an insulating substrate, producing micron-sized graphene sheets with thicknesses down to a single atomic layer (*4*–*8*). Thus far, research on these thin graphene sheets has focused primarily on their electronic properties. We demonstrate a method of suspending single- and multilayer graphene sheets over trenches and show that such sheets can be mechanically actuated. This work also makes a detailed study of the mechanical properties of these graphene resonators, including resonance frequency, spring constant, built-in tension, and quality factor.

Suspended graphene sheets are fabricated with a peeling process similar to that reported previously (*5*–*7*). In our case, the graphene sheets are mechanically exfoliated over predefined trenches etched into a SiO_2 surface (Fig. 1) (*9*). The result is a micron-scale doubly clamped beam or cantilever clamped to the SiO_2 surface by van der Waals attraction. Some devices have prepatterned gold electrodes between the trenches to make electrical contact (Fig. 1, A and D).

A noncontact mode atomic force microscope (AFM) was used to quantitatively measure the thickness of the sheets on the substrate next to the trench, as shown in the inset in Fig. 1D. However, for sheets thinner than 2 to 3 nm, such measurements are unreliable (*10*–*12*). For these we used spatially resolved Raman spectroscopy to determine the number of layers (Fig. 1C) (*10*–*12*). The graphene sheet in Fig. 1B has an AFM-determined height of 0.9 nm. By comparison with previous results (*10*–*12*), the shape of the Raman peak near 2700 cm^{-1} suggests the sheet is two layers thick over the area lying on the SiO_2 substrate (Fig. 1C), whereas the section suspended over the trench is a single graphene layer.

All resonator measurements are performed at room temperature and a pressure of $<10^{-6}$ torr unless otherwise indicated. The resonators are actuated by using either electrical (Fig. 1A) or optical modulation. In the case of electrical modulation, a time-varying radio frequency (rf)

[1]Cornell Center for Materials Research, Cornell University, Ithaca, NY 14853, USA. [2]Pomona College, Department of Physics, Claremont, CA 91711, USA.

*To whom correspondence should be addressed. E-mail: mceuen@ccmr.cornell.edu

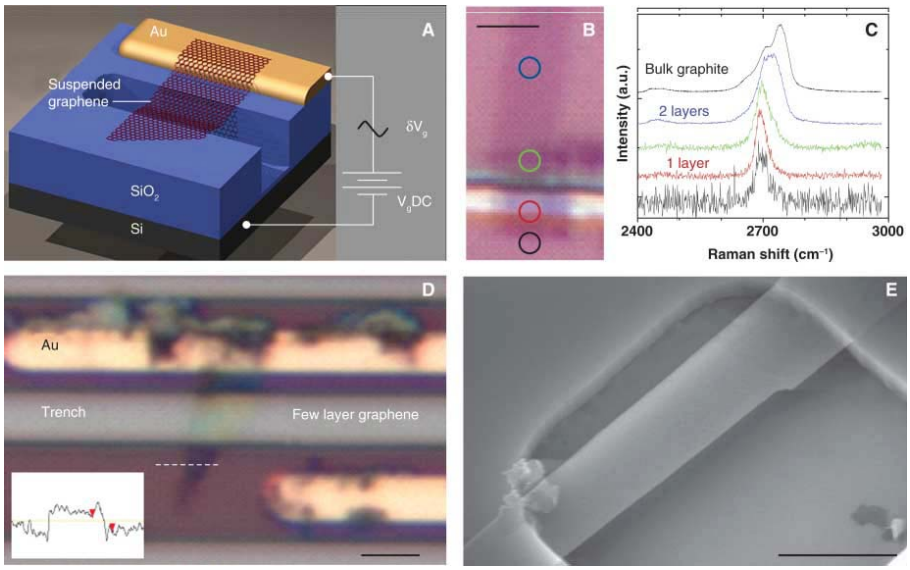

Fig. 1. (**A**) Schematic of a suspended graphene resonator. (**B**) An optical image of a double-layer graphene sheet that becomes a single suspended layer over the trench. Scale bar, 2 μm. Each colored circle corresponds to a point where a Raman spectrum was measured. (**C**) Raman signal from a scan on the graphene piece. Each colored scan is data taken at each of the matching colored circles. The top scan is used as a reference and corresponds to the Raman shift of bulk graphite. (**D**) An optical image of few-layer (~4) graphene suspended over a trench and contacting a gold electrode. Scale bar, 1 μm. (Inset) A line scan from tapping mode AFM corresponding to the dashed line in the optical image. It shows a step height of 1.5 nm. (**E**) A scanning electron microscope image of a few-layer (~2) graphene resonator. Scale bar, 1 μm.

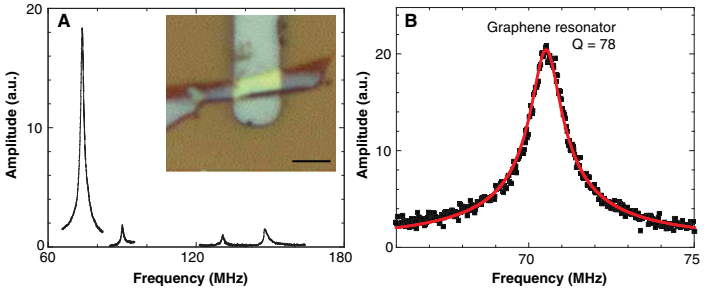

Fig. 2. (**A**) Amplitude versus frequency for a 15-nm-thick multilayer graphene resonator taken with optical drive. (Inset) An optical image of the resonator. Scale bar, 5 μm. (**B**) Amplitude versus frequency taken with optical drive for the fundamental mode of the single-layer graphene resonator shown in Fig. 1B. A Lorentzian fit of the data is shown in red.

voltage δV_g at frequency f is superimposed on top of a constant voltage and applied to the graphene sheet. The result is an electrostatic force between the suspended graphene sheet and the substrate

$$F_{el} \approx 1/2\ C_g'(V_g^{dc})^2 + C_g' V_g^{dc}\ \delta V_g \qquad (1)$$

where C_g' is the derivative of the gate capacitance with respect to the distance to the gate, and V_g^{dc} and δV_g are, respectively, the dc and time-varying rf voltages applied to the gate (*13*). For optical actuation, the intensity of a diode laser focused on the sheet is modulated at frequency f, causing a periodic contraction/expansion of the layer that leads to motion. In both cases, the motion is detected by monitoring the reflected light intensity from a second laser with a fast photodiode (*9*).

Figure 2A shows the measured amplitude versus frequency for a 15-nm-thick sheet suspended over a 5-μm trench. Multiple resonances are observed, the most prominent one at the lowest frequency. We associate this dominant peak with the fundamental vibrational mode; its detected intensity is largest when the motion is in-phase across the entire suspended section. We will limit our discussion primarily to this fundamental mode. A fit to a Lorentzian yields a resonant frequency f_o = 42 MHz and a quality factor Q = 210. Figure 2B shows similar results for the single-layer graphene resonator from Fig. 1B; f_0 = 70.5 MHz and Q = 78. Figure 3 shows the results of measurements of 33 resonators with thicknesses varying from a single atomic layer to sheets 75 nm thick. The frequency f_0 of the fundamental modes varies from 1 MHz to 170 MHz, with quality factor Q of 20 to 850.

For mechanical resonators under tension T, the fundamental resonance mode f_0 is given by

$$f_0 = \{[A\ (E/\rho)^{1/2}\ t\ /\ L^2]^2 + A^2 0.57 T\ /\ \rho L^2 wt\}^{1/2} \qquad (2)$$

where E is the Young's modulus; ρ is the mass density; t, w, and L are the dimensions of the suspended graphene sheet; and the clamping coefficient, A, is 1.03 for doubly clamped beams and 0.162 for cantilevers (*14*). In the limit of small tension, Eq. 2 predicts that the resonance frequency f_0 scales as t/L^2. Figure 3A shows the resonant frequency of the fundamental mode for resonators with t > 7 nm as a function of t/L^2 plotted as filled squares. Also plotted is the theoretical prediction, Eq. 2, in the limit of zero tension, for both cantilevers and beams, where we have used the known values for bulk graphite ρ = 2200 kg/m^3 and E = 1.0 TPa (*3*). This is a valid comparison considering the extensive theoretical and experimental work that shows the basal plane of graphite to have a similar value for E as graphene and carbon nanotubes (*3*, *15*). To account for possible errors in E, we plot

dashed lines that correspond to values of $E = 0.5$ TPa and 2 TPa. The data follow the predictions reasonably accurately, indicating that thicker resonators are in the bending-dominated limit with a modulus E characteristic of the bulk material. This is among the highest modulus resonators to date, greater than 53 to 170 GPa in 12- to 300-nm-thick Si cantilevers and similar to single-walled carbon nanotubes and diamond NEMS (*13, 16, 17*). In contrast to ultrathin Si cantilevers, the graphene resonators show no degradation in Young's modulus with decreasing thickness (*17*).

The resonant frequencies versus t/L^2 for the resonators with $t < 7$ nm are shown as open squares in Fig. 3A. The frequencies of these thinner resonators show more scatter, with the majority having resonant frequencies higher than predicted by bending alone. A likely explanation for this is that many of the resonators are under tension, which increases f_0 (see supporting online text). The tension likely results from the fabrication process, where the friction between the graphite and the oxide surface during mechanical exfoliation stretches the graphene sheets across the trench.

The single-layer graphene resonator shown in Fig. 1B illustrates the importance of tension in the thinnest resonators. It has a fundamental frequency $f_0 = 70.5$ MHz, much higher than the 5.4 MHz frequency expected for a tension-free beam with $t = 0.3$ nm, $L = 1.1$ μm, and $w = 1.93$ μm. From Eq. 2, this implies that the graphene resonator has a built-in tension of $T = 13$ nN. From the expression $\Delta L/L = T/(EA)$, this corresponds to a strain of 2.2×10^{-3}%.

An important measure of any resonator is the normalized width of the resonance peak characterized by the quality factor $Q = f_0/\Delta f$. A high Q is essential for most applications because it increases the sensitivity of the resonator to external perturbation. A plot of the Q versus the thickness for all the graphene resonators (Fig. 3B) shows that there is no clear dependence of Q on thickness. This contrasts with results on thicker NEMS resonators fabricated from silicon (*18*). The quality factors at room temperature are lower than diamond NEMS (2500 to 3000) of similar volume and significantly lower than high-stress Si_3N_4 nanostrings (200,000), yet similar to those reported in single-walled carbon nanotubes (50 to 100) (*13, 16, 19*). Preliminary studies on a 20-nm-thick resonator found a dramatic increase in Q with decreasing temperature ($Q = 100$ at 300 K to $Q = 1800$ at 50 K). This suggests that high Q operation of graphene resonators should be possible at low temperatures.

Even when a resonator is not being driven, it will still oscillate due to thermal excitation by a root mean square (RMS) amount $x_{th} = [k_B T/\kappa_{eff}]^{1/2}$, where $\kappa_{eff} = m_{eff}\,\omega_0^2 = 0.735 Lwt\rho\omega_0^2$ is the effective spring constant of the mode (*2*). An example is shown in Fig. 4A, where a 5-nm-thick resonator with $f_0 = 35.8$ MHz and $\kappa_{eff} = 0.7$ N/m has a room-temperature thermal RMS motion of $x_{th} = 76$ pm. For resonators for which the thermal vibrations can be measured, we use this thermal RMS motion to scale the measured photodetector voltage with resonator displacement (see supporting online text). Figure 4B shows such a rescaled plot of the displacement amplitude versus rf drive voltage. The resonator is linear up to displacements of 3 nm, or on the order of its thickness, where nonlinearities associated with additional tension are known to set in (*2*). This nonlinearity is characterized as a deviation from a linear increase in amplitude with driving force and accompanied by a decrease in Q (Fig. 4B).

Two applications of nanomechanical resonators are ultralow mass detection (see supporting online text) and ultrasensitive force detection. The ultimate limit on the force sensitivity is set by the thermal fluctuations in the resonator:

$$dF^f = [4\,\kappa_{eff}\,(k_B\,T)/Q\,\omega_0]^{1/2} \qquad (3)$$

For the resonator in Fig. 4A, this results in a force sensitivity of 0.9 fN/Hz$^{1/2}$. From Eq. 1, this corresponds to a charge sensitivity of $dQ^f = dF^f\,d/V_g^{dc} = 8 \times 10^{-4}$ e/Hz$^{1/2}$, where d is the distance between the graphene sheet and the gate electrodes. This is a high sensitivity demonstrated at room temperature; at low temperatures, with the onset of higher quality factors, it could rival those of rf single-electron transistor electrometers (1×10^{-5} e/Hz$^{1/2}$) (*20, 21*). The high Young's modulus, extremely low mass, and large surface area make these resonators ideally suited

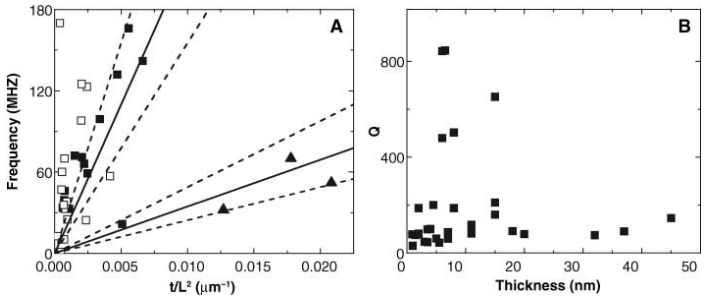

Fig. 3. (**A**) A plot showing the frequency of the fundamental mode of all the doubly clamped beams and cantilevers versus t/L^2. Cantilevers, triangles; doubly clamped beams with $t > 7$ nm, filled squares; doubly clamped beams with $t < 7$ nm, open squares. All thicknesses are determined by AFM. The solid line is the theoretical prediction with no tension and $E = 1$ TPa. The dashed lines correspond to $E = 0.5$ TPa and 2 TPa. (**B**) The quality factor of the fundamental mode versus thickness for all resonators measured.

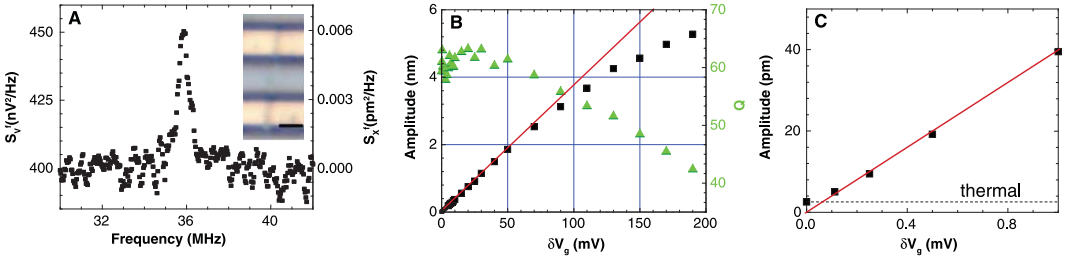

Fig. 4. (**A**) Noise power density versus frequency taken at a resolution bandwidth of 1 kHz. (Inset) An optical image of the resonator. The resonator has dimensions $t = 5$ nm, $L = 2.7$ μm, and $w = 630$ nm. Scale bar, 2 μm. (**B**) Amplitude of resonance and quality factor versus δV_g for $V_g^{dc} = 2$ V. (**C**) Expanded view of (B) for small δV_g.

for use as mass, force, and charge sensors (*22*–*28*). The application of graphene NEMS extends beyond just mechanical resonators. This robust conducting membrane can act as a nanoscale supporting structure or atomically thin membrane separating two disparate environments.

References and Notes

1. H. G. Craighead, *Science* **290**, 1532 (2000).
2. K. L. Ekinci, M. L. Roukes, *Rev. Sci. Instrum.* **76**, 061101 (2005).
3. B. T. Kelly, *Physics of Graphite* (Applied Science, London; Englewood, NJ, 1981).
4. M. Wilson, *Phys. Today* **59**, 21 (2006).
5. K. S. Novoselov *et al.*, *Proc. Natl. Acad. Sci. U.S.A.* 10451 (2005).
6. K. S. Novoselov *et al.*, *Nature* **438**, 197 (2005).
7. Y. B. Zhang, Y. W. Tan, H. L. Stormer, P. Kim, *Nature* **438**, 201 (2005).
8. J. S. Bunch, Y. Yaish, M. Brink, K. Bolotin, P. L. McEuen, *Nano Lett.* **5**, 287 (2005).
9. Materials and methods are available as supporting material on *Science* Online.
10. A. C. Ferrari *et al.*, *Phys. Rev. Lett.* **97**, 187401 (2006).
11. A. Gupta, G. Chen, P. Joshi, S. Tadigadapa, P. C. Eklund, *Nano Lett.* **6**, 2667 (2006).
12. D. Graf *et al.*, http://arxiv.org/PS_cache/cond-mat/pdf/0607/0607562.pdf (2006).
13. V. Sazonova *et al.*, *Nature* **431**, 284 (2004).
14. S. Timoshenko, D. H. Young, W. Weaver, *Vibration Problems in Engineering*. (Wiley, New York, ed. 4, 1974), pp. 425–427.
15. D. Qian, G. J. Wagner, W. K. Liu, M. F. Yu, R. S. Ruoff, *Appl. Mech. Rev.* **55**, 495 (2002).
16. L. Sekaric *et al.*, *Appl. Phys. Lett.* **81**, 4455 (2002).
17. X. X. Li, T. Ono, Y. L. Wang, M. Esashi, *Appl. Phys. Lett.* **83**, 3081 (2003).
18. K. Y. Yasumura *et al.*, *J. Microelectromech. Syst.* **9**, 117 (2000).
19. S. S. Verbridge, J. M. Parpia, R. B. Reichenbach, L. M. Bellan, H. G. Craighead, *J. Appl. Phys.* **99**, 124304 (2006).
20. R. J. Schoelkopf, P. Wahlgren, A. A. Kozhevnikov, P. Delsing, D. E. Prober, *Science* **280**, 1238 (1998).
21. M. D. LaHaye, O. Buu, B. Camarota, K. C. Schwab, *Science* **304**, 74 (2004).
22. B. Ilic *et al.*, *J. Appl. Phys.* **95**, 3694 (2004).
23. N. V. Lavrik, P. G. Datskos, *Appl. Phys. Lett.* **82**, 2697 (2003).
24. K. L. Ekinci, X. M. H. Huang, M. L. Roukes, *Appl. Phys. Lett.* **84**, 4469 (2004).
25. T. Kenny, *IEEE Sensors J.* **1**, 148 (2001).
26. A. N. Cleland, M. L. Roukes, *Nature* **392**, 160 (1998).
27. R. G. Knobel, A. N. Cleland, *Nature* **424**, 291 (2003).
28. T. P. Burg, S. R. Manalis, *Appl. Phys. Lett.* **83**, 2698 (2003).

29. We thank C. Umbach and L. Bellan for help with Raman spectroscopy; R. Reichenbach for help with the laser setup and the schematic in the Supporting Online Material; and P. Kim, Y. Zhang, R. Ilic, and K. Schwab for useful discussions. This work was supported by the NSF through the Center for Nanoscale Systems and the Cornell Center for Materials Research, and by the Microelectronics Advanced Research Corporation Focused Research Center on Materials, Structures, and Devices. Sample fabrication was performed at the Cornell Nanoscale Science and Technology Facility, a National Nanotechnology Infrastructure Network node, funded by NSF.

Supporting Online Material

www.sciencemag.org/cgi/content/full/315/5811/490/DC1
Materials and Methods
SOM Text
Figs. S1 to S3
References

27 October 2006; accepted 11 December 2006
10.1126/science.1136836

Improved Oxygen Reduction Activity on $Pt_3Ni(111)$ via Increased Surface Site Availability

Vojislav R. Stamenkovic,[1,2]* Ben Fowler,[3] Bongjin Simon Mun,[2] Guofeng Wang,[4] Philip N. Ross,[2] Christopher A. Lucas,[3] Nenad M. Marković[1]*

The slow rate of the oxygen reduction reaction (ORR) in the polymer electrolyte membrane fuel cell (PEMFC) is the main limitation for automotive applications. We demonstrated that the $Pt_3Ni(111)$ surface is 10-fold more active for the ORR than the corresponding Pt(111) surface and 90-fold more active than the current state-of-the-art Pt/C catalysts for PEMFC. The $Pt_3Ni(111)$ surface has an unusual electronic structure (*d*-band center position) and arrangement of surface atoms in the near-surface region. Under operating conditions relevant to fuel cells, its near-surface layer exhibits a highly structured compositional oscillation in the outermost and third layers, which are Pt-rich, and in the second atomic layer, which is Ni-rich. The weak interaction between the Pt surface atoms and nonreactive oxygenated species increases the number of active sites for O_2 adsorption.

When a polymer electrolyte membrane fuel cell (PEMFC) is used in a demanding application such as an automobile, it must overcome the kinetic limitations on the oxygen reduction reaction (ORR), which have led to three fundamental problems (*1*–*5*). First, the substantial overpotential for the ORR (*6*–*10*) at practical operating current densities reduces the thermal efficiency well below the thermodynamic limits, typically to about 43% at 0.7 V [versus the theoretical thermal efficiency of 83% at the reversible potential for the ORR (1.23 V)]. Second, an approximately fivefold reduction of the amount of Pt (platinum-loading) in current PEMFC stacks is needed to meet the cost requirements for large-scale automotive applications (*10*). Finally, the dissolution and/or loss of Pt surface area in the cathode must be greatly reduced.

These limitations could be eliminated if stable cathode catalysts, with an order of magnitude increase in the specific activity over that of state-of-the-art Pt/C catalysts, can be developed (*10*). In the hope that a combination of different metals would have improved catalytic activity and stability relative to those of a pure metal, the ORR has been studied on numerous bi- or multimetallic alloys (*6*, *8*, *11*–*17*). These studies have led to incremental improvements to catalyst performance, but large increases in activity have yet to be realized.

Rather than use a trial-and-error or combinatorial approach, we have examined selected cathode materials with well-characterized surfaces so that the mechanism of action can be attributed to a specific property (at the atomic and molecular level) of the surface under study. In this way, we can determine (i) whether the kinetics of the ORR are structure-sensitive, (ii) the composition of the topmost surface atomic layers (the segregation profile), and (iii) how alloying [usually described in terms of the ligand effect or/and ensemble effect (*18*–*20*)] alters the chemical properties of the surfaces. Similar approaches are commonly used in gas-phase catalysis (*21*) under ultrahigh vacuum (UHV) and near-ambient conditions, but alloy surface chemistry on single-crystal surfaces at electrochemical interfaces is relatively unexplored. These aqueous interfaces are more complex in that they necessarily contain solvent and electronic/ionic charge, and (experimentally) it is very challenging but still tractable to use in situ surface-sensitive methods to characterize potential-induced changes in the surface properties and reactivity.

We have used a combination of ex situ and in situ surface-sensitive probes and density functional theory (DFT) calculations to study the ORR on $Pt_3Ni(hkl)$ single-crystal surfaces, identify which surface properties govern the variations in reactivity of PtNi catalysts, and determine how surface structures, surface segregation, and intermetallic bonding affect the ORR kinetics. Well-characterized PtNi single-crystal electrode surfaces were formed and characterized with UHV methods for surface preparation and surface analysis. These surfaces were transferred into the electrochemical environment without airborne contamination, and the stability of the UHV-prepared

[1]Materials Science Division, Argonne National Laboratory, Argonne, IL 60439, USA. [2]Materials Sciences Division, Lawrence Berkeley National Laboratory, University of California, Berkeley, CA 94720, USA. [3]Oliver Lodge Laboratory, Department of Physics, University of Liverpool, Liverpool, L69 7ZE, UK. [4]Department of Chemistry and Physics, University of South Carolina, Aiken, SC 29801, USA.

*To whom correspondence should be addressed. E-mail: vrstamenkovic@anl.gov (V.R.S.); nmmarkovic@anl.gov (N.M.M.)

Appendix B

Mechanical Properties of Suspended Graphene Sheets.

Mechanical properties of suspended graphene sheets

I. W. Frank and D. M. Tanenbaum[a)]
Pomona College, Department of Physics and Astronomy, Claremont, California 91711

A. M. van der Zande and P. L. McEuen
Cornell Center for Materials Research, Cornell University, Ithaca, New York 14853

(Received 10 June 2007; accepted 27 August 2007; published 11 December 2007)

Using an atomic force microscope, we measured effective spring constants of stacks of graphene sheets (less than 5) suspended over photolithographically defined trenches in silicon dioxide. Measurements were made on layered graphene sheets of thicknesses between 2 and 8 nm, with measured spring constants scaling as expected with the dimensions of the suspended section, ranging from 1 to 5 N/m. When our data are fitted to a model for doubly clamped beams under tension, we extract a Young's modulus of 0.5 TPa, compared to 1 TPa for bulk graphite along the basal plane, and tensions on the order of 10^{-7} N. © *2007 American Vacuum Society.* [DOI: 10.1116/1.2789446]

I. INTRODUCTION

Nanoelectromechanical systems (NEMSs) have many applications in fundamental science and engineering, such as the study of quantum limited motion,[1] mass detection,[2,3] and force detection.[4] In all of these applications, it is extremely beneficial to have the active element have as low of a mass as possible and as high of a quality factor as possible.[5] Materials such as Si, SiO_2 SiN, SiC, diamond, and GaAs have been studied with the prototypical resonator consisting of a nanoscale beam clamped on one or both ends.[6] Graphite appears to be an excellent material for the fabrication of NEMS resonators. Its makeup of strongly bonded planar sheets held together by weak van der Waals interactions makes it relatively simple to fabricate extremely thin resonators, even down to the natural limit of one atomic layer. Graphene, like carbon nanotubes, is extremely strong and stiff compared to silicon based materials. Beyond its material strength, graphene is advantageous due its tunable electronic properties, chemical inertness, and high thermal conductivity.[7]

Before suspended graphene sheets can become the basis for any practical NEMS sensors, their mechanical properties must be measured as they may deviate from the known properties of the bulk graphite. Using atomic force microscopy (AFM), we are able to accurately measure the length, width, and thickness of suspended stacks of graphene sheets. By pressing on the suspended sheets with AFM tips with calibrated spring constants, we are able extract the spring constants of the sheets. By examining how the spring constants vary with the size dimensions of the suspended sheets, we are able to extract built-in axial tensions and the Young's modulus of the graphene layers.

II. BACKGROUND

We have previously reported that suspended graphene sheets can be resonated in vacuum[8] with an optical detection setup using either a modulated blue laser that locally heats the sample,[3] or a capacitive drive using a varying potential between the silicon backplane and the suspended graphite.[9] This dynamic method allows for highly accurate measurements of the resonant frequencies, but it is nontrivial to determine the absolute amplitude of the motion. While this can be accomplished by examining the thermal noise, it is not a direct measurement and the calibration is different each time a sample is mounted in the detection system. In contrast, static AFM deflection measurements provide a simple and direct measurement of both displacement and force for the determination of spring constants.

In our previous work on dynamic measurements, we modeled the resonators as doubly clamped beams in the limit of small tension.[8] As was noted in this work, it is likely that tension matters, particularly for the thinnest samples. The equation determining the fundamental natural frequency (hertz) of a doubly clamped beam under tension is

$$f = 1.03\sqrt{\frac{Et^2}{\rho L^4} + \frac{T}{3.4mL}}, \tag{1}$$

where T is the tension in the beam, E is the Young's modulus, ρ is the density of the material, m is the effective mass, and t and L are the thickness and length of the beam, respectively. The numerical constants are determined by clamping conditions.[10,11] Using the relation $f=(1/2\pi)\sqrt{k/m}$, where k is the effective spring constant of the beam, we can solve for k. The resulting equation is

$$k = 30.78Ew(t/L)^3 + 12.32(T/L), \tag{2}$$

where w is the width of the beam.

In the case of static deflection measurements, the distribution of the load is from a point contact rather than along the beam as in the dynamic measurements of resonators. Thus, while the functional form is the same with contributions from both bending and tension, the constants are not. For a doubly clamped beam in equilibrium with a static force applied at the center of the beam and under axial tension, the resulting equation is

[a)]Electronic mail: dtanenbaum@pomona.edu

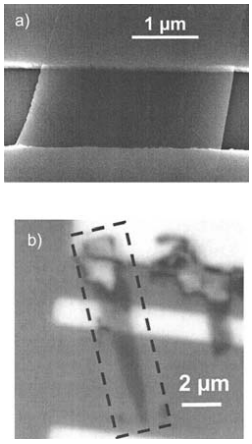

FIG. 1. (a) A SEM micrograph of a graphene sheet suspended above a trench (horizontal stripe) etched in silicon dioxide. The sheet measured 7 nm thick by AFM. (b) An optical micrograph of a different suspended few-layer graphene sheet measured to be 2 nm thick by AFM.

$$k = 16.23Ew(t/L)^3 + 4.93T/L. \quad (3)$$

This expression holds until the deflection moves beyond the linear regime in Hooke's law due to the stretching of the beam.[12,13]

III. FABRICATION AND YIELD

Suspended stacks of graphene are obtained by mechanically exfoliating kish graphite[14] across photolithographically patterned trenches that act analogous to a cheese grater and shear off thin sheets of the graphite.[8,15–18] The graphite sheets can be up to 50 nm thick and as thin as a single layer of atoms. Their length and width are largely determined by the size of the trenches and are generally between 0.5 and 5 μm. Kish graphite comes in flakes that are a few millimeters on a side. These flakes are then attached to a probe which acts as a "pencil." The graphite is cleaved, exposing an atomically smooth surface on the tip of the pencil. The pencil is then rubbed across the silicon oxide substrate, mechanically exfoliating pieces of graphite onto the surface.

The key to this production technique is in selecting the thickness of the dielectric that the sheets of graphite are resting on. With the correct thickness of the oxide (280 nm as measured by thin film interferometry), the very thin suspended graphene sheets show up in vivid shades of purple in an optical microscope.[19] The hue of the graphite can be correlated with its thickness and allows for a quick determination of graphene sheets, meriting further characterization with an AFM. Figures 1(a) and 1(b) are a scanning electron microscope (SEM) and an optical micrograph of suspended graphene sheets, respectively.

Once the desired pieces have been selected optically, more accurate measurements are performed with an AFM (Ref. 20) in ac mode to provide the width and length of the suspended graphite with nanometer resolution. AFM was used in ac mode to image the suspended graphene sheets as it is less likely to cause damage than contact mode. For sheets thinner than 2–3 nm, the measurement of the thickness with AFM is unreliable for determining the number of graphene layers so Raman spectroscopy is used to get an accurate count.[21–23]

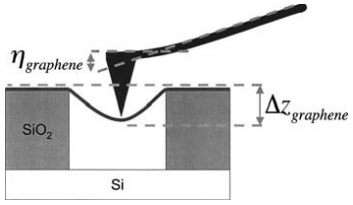

FIG. 2. A schematic of an AFM tip that is deflected while pushing down on a suspended graphene sheet. η_{graphene} is measured by the AFM and $\Delta z_{\text{graphene}}$ is calculated using Eq. (4).

In contrast to the fabrication of oscillators made from suspended carbon nanotubes that display significant slack,[9] all the suspended graphene sheets made via exfoliation appear to be under tension. This tension can be increased by applying a dc bias between the suspended graphite and the silicon backplane which can be used to tune the resonance frequency of the suspended graphene layers.[8,9]

IV. STATIC DEFLECTION MEASUREMENTS

Static deflection measurements are made by acquiring force distance curves with an AFM. Once the dimensions of the suspended graphene layers have been measured by AFM, the tip is pushed down in the center of the beam in ac mode, and both amplitude and deflection signals are recorded versus z_{piezo}.[24,25] Figure 2 is a schematic of an AFM tip pushing down on suspended graphene layers. From the deflection of the tip as it pushes down on the suspended sheet, we are able to extract the effective spring constant (k) of the suspended graphene layers. It is important that the spring constant of the tip be close to that of the graphite sheets or an accurate measurement becomes impossible. If the tip is too stiff in comparison to the graphene layers, it will not deflect a detectable amount. If the tip is too soft, the sheets will appear to be rigid and no meaningful information can be extracted from the measurement. We used tips with a nominal spring constant of 2 N/m.[26] These are 240 μm long silicon cantilevers designed for ac mode. Each tip's spring constant is individually calibrated using a reference cantilever with a known spring constant.[27] The calibration process involves comparing the results of pushing the AFM tip against an immovable surface and the reference cantilevers, following the approach of Tortonese and Kirk.[28] Once the spring constant of the tips are known, the suspended graphene sheet's spring constant can be measured. The tip is pushed slowly ($\sim$100 nm/s) against the sheets in order to minimize damage to the tip and the graphite, and a curve of the tip displacement versus the position of the piezo is obtained [see Fig.

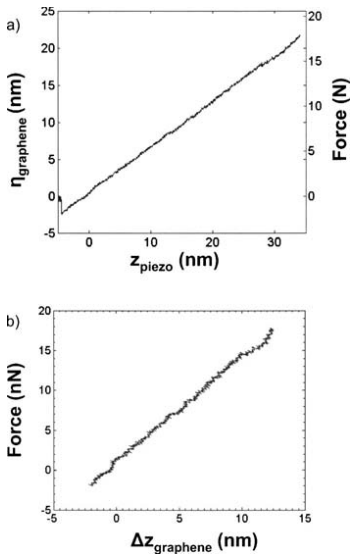

FIG. 3. (a) On the left axis is the curve obtained by the AFM while pushing down on a suspended graphene sheet. The right axis is the corresponding force. (b) Graph of force vs displacement of the suspended sheet. The spring constant of the sheet is the slope of these data.

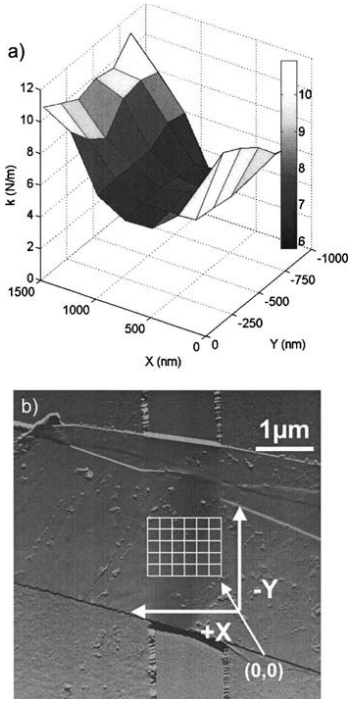

FIG. 4. (a) A surface plot of the spring constant of a suspended graphene sheet vs the location of the AFM tip. (b) An amplitude AFM micrograph of the suspended sheet measured to obtain (a) and imaged in by SEM in Fig. 1(a). Each data point was taken at the intersection of the grid located on the suspended portion of the graphene. The trench etched into the silicon dioxide is seen as a vertical stripe.

3(a)]. As the AFM tip comes into contact with the suspended graphene device, the free amplitude of the ac motion of the tip cantilever goes to zero, and the cantilever is pulled down onto the surface, resulting in the initial dip in the deflection seen in Fig. 3(a). Using our measured spring constant of the tip, we are able to extract a graph of the force exerted on the tip versus the displacement of the graphene sheets [see Fig. 3(b)]. We calculate the displacement using

$$z_{\text{piezo}} = \eta_{\text{graphene}} + \Delta z_{\text{graphene}}, \tag{4}$$

where η_{graphene} is the deflection of the tip measured by the AFM, z_{piezo} is location of the piezos moving the tip, and $\Delta z_{\text{graphene}}$ is the deflection of the suspended layers of graphene. In the regime of small displacements—on the order of the thickness of the layers—this curve will be linear [see Fig. 3(b)] and through Hooke's law the slope will yield the effective spring constant of the suspended graphene sheets. Using this technique, we measured spring constants of 1–5 N/m in suspended sheets with thicknesses from 2 to 8 nm.

It is an interesting question how the spring constant changes over the length and width of the sheet, and what can be termed the center of the beam, especially since many of the sheets are of trapezoidal shape with slightly varying thicknesses across the suspended portion. Some spatial scans of the sheets, an example of which is displayed in Fig. 4(a), measuring the spring constant at various points, show that the spring constant of the suspended sheets rises by over a factor of 2 nearer the clamped edges and falls of slightly nearer the free edges, making a saddle point of the spring constant in the center. However, in the center, the effect is fairly small; so long as the tip is within 100 nm of the center of a 1 μm long suspended sheet, the spring constant is set within the reproducibility of the measurements.

V. DISCUSSION

In Fig. 5 we plot spring constants for eight different suspended graphene sheets versus the quantity $w(t/L)^3$, the dependence of the directly measured quantities in the bending term, from Eq. (3). Although the tension term in Eq. (3) is important for our suspended graphene sheets, we note that L was similar in all the sheets we measured and the $w(t/L)^3$ term is expected to vary much more than the T/L term. As a result, in our analysis we model the T/L term as a constant offset to a linear fit of k vs $w(t/L)^3$. This assumes that all the sheets have similar tensions; however, given the linear nature of our data, plotted in Fig. 5, this appears to be a good approximation.

Figure 5 shows that one of our 2 nm thick graphene sheets does not fall near our linear fit of all the data shown as

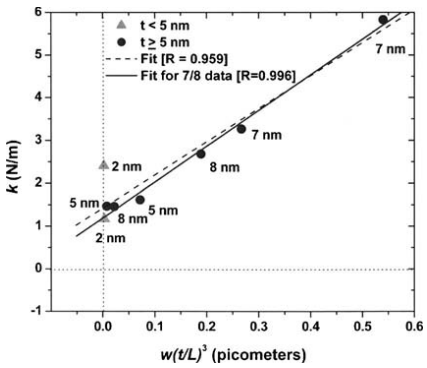

FIG. 5. A plot of the spring constant as measured in the center of the suspended region of the graphene sheets, vs $w(t/L)^3$ for eight different samples. From the linear fit, we are able to extract an average tension and a Young's modulus. The dashed line is the fit to all the data points, whereas the solid line is the fit for 7/8 of the data.

a dashed line in Fig. 5. This could be due to many factors including the unusually high tension, loss of rigidity in the beam, or different clamping conditions. As a result, we focus our discussion on the measurements made on the remaining seven data points fitted as the solid line in Fig. 5. The slope of this solid line suggests an E of 0.5 TPa, compared to the 1 TPa value for bulk graphite.[7] Using the offset of the linear fit and an average L, we obtain a tension of 300 nN, suggesting that the tension in all the sheets is on the order of hundreds of nanonewtons. Calculations with each individual device's length suggest this to be accurate.

VI. CONCLUSION

We have performed static and dynamic measurements of the mechanical properties of nanometer-thick suspended graphite sheets made by exfoliating thin layers of graphite over trenches patterned in silicon dioxide films on a silicon substrate. We present a simple, direct, and nondestructive approach for obtaining the mechanical properties of atomically thin membranes with AFM. In contrast to other techniques, this approach has spatial resolution on the nanometer scale and can map properties across a membrane. In contrast to NEMS based on molecules such as DNA and carbon nanotubes, membranes of graphene can be used as barriers between different environments, and the technique presented can be adapted to work in vacuum or fluid cells. Spring constants ranging from 1 to 5 N/m were observed for suspended graphene sheets less than 10 nm thick. Fitting to the model of a doubly clamped beam in equilibrium with a static force and under axial tension, we extracted a Young's modulus of 0.5 TPa, significantly below the bulk value of 1 TPa, and tensions of hundreds of nanonewtons. For one of our eight sheets, the behavior is erratic and is only a loose fit to our model.

ACKNOWLEDGMENTS

The authors would like to thank the NSF for support through the Cornell Center for Materials Research, the Cornell Center for Nanoscale Systems, and the Cornell Nano-Scale Facility, a member of the National Nanotechnology Infrastructure Network. Additionally the authors would like to thank Leon Bellan, Scott Bunch, Scott Verbridge, Scott Berkley, Jeevak Parpia, and Harold Craighead for helpful discussions and support.

[1] M. LaHaye, O. Buu, B. Camarota, and K. Schwab, Science **304**, 74 (2004).
[2] K. Ekinci, Y. Yang, and M. Roukes, J. Appl. Phys. **95**, 2682 (2004).
[3] B. Ilic, J. Appl. Phys. **95**, 3694 (2004).
[4] D. Rugar, R. Budakian, H. Mamin, and B. Chui, Nature (London) **430**, 329 (2004).
[5] H. Craighead, Science **290**, 1532 (2000).
[6] K. Ekinci and M. Roukes, Rev. Sci. Instrum. **76**, 061101 (2005).
[7] B. Kelly, *Physics of Graphite* (Applied Science, Englewood, NJ, 1981).
[8] J. S. Bunch, A. M. van der Zande, S. S. Verbridge, I. W. Frank, D. M. Tanenbaum, J. M. Parpia, H. G. Craighead, and P. L. McEuen, Science **315**, 490 (2007).
[9] V. Sazonova, Y. Yaish, H. Uestuenel, D. Roundy, T. A. Arias, and P. L. McEuen, Nature (London) **431**, 284 (2004).
[10] S. C. Jun, X. Huang, M. Manolidis, C. Zorman, M. Mehregany, and J. Hone, Nanotechnology **17**, 1506 (2006).
[11] W. Weaver, S. P. Timoshenko, and D. H. Young, *Vibration Problems in Engineering*, 5th Ed. (Wiley, New York, 1990), p. 454.
[12] M. W. Pruessner, T. T. King, D. P. Kelly, R. Grover, L. C. Calhoun, and R. Ghodssi, Sens. Actuators, A **105**, 190 (2003).
[13] S. D. Senturia, *Microsystem Design* (Kluwer Academic, Boston, MA, 2000), p. 249.
[14] Purchased from Toshiba Ceramics.
[15] J. S. Bunch, Y. Yaish, M. Brink, K. Bolotin, and P. L. McEuen, Nano Lett. **5**, 287 (2005).
[16] K. Novoselov, D. Jiang, F. Schedin, T. Booth, V. Khotkevich, S. Morozov, and A. Geim, Proc. Natl. Acad. Sci. U.S.A. **102**, 10451 (2005).
[17] K. S. Novoselov, A. K. Geim, S. V. Morozov, D. Jiang, M. I. Katsnelson, I. V. Grigorieva, S. V. Dubonos, and A. A. Firsov, Nature (London) **438**, 197 (2005).
[18] Y. Zhang, Y. W. Tan, H. L. Stormer, and P. Kim, Nature (London) **438**, 201 (2005).
[19] P. Blake, K. Novoselov, A. H. C. Neto, D. Jiang, R. Yang, T. Booth, A. Geim, and E. Hill, Appl. Phys. Lett. **91**, 063124 (2007).
[20] We used a Dimension 3000 AFM from Digital Instruments.
[21] A. C. Ferrari, J. C. Meyer, V. Scardaci, C. Casiraghi, M. Lazzeri, F. Mauri, S. Piscanec, D. Jiang, K. S. Novoselov, S. Roth, and A. K. Geim, Phys. Rev. Lett. **97**, 187401 (2006).
[22] A. Gupta, G. Chen, P. Joshi, S. Tadigadapa, and P. C. Eklund, Nano Lett. **6**, 2667 (2006).
[23] D. Graf, F. Molitor, K. Ensslin, C. Stampfer, A. Jungen, C. Hierold, and L. Wirtz, Nano Lett. **7**, 238 (2007).
[24] J. D. Whittaker, E. D. Minot, D. M. Tanenbaum, P. L. McEuen, and R. C. Davis, Nano Lett. **6**, 953 (2006).
[25] E. Minot, Y. Yaish, V. Sazonova, J. Y. Park, M. Brink, and P. L. McEuen, Phys. Rev. Lett. **90**, 156401 (2003).
[26] Olympus AC-240TS.
[27] Purchased from Veeco Metrology; calibration performed with Laser Doppler Vibrometry by B.Ohler as per Application Note 94, Veeco Instruments, Inc. (2007).
[28] M. Tortonese and M. Kirk, Proc. SPIE **3009**, 53 (1997).

Appendix C

Recipes & Process Flows

C.1 Optical Lithography

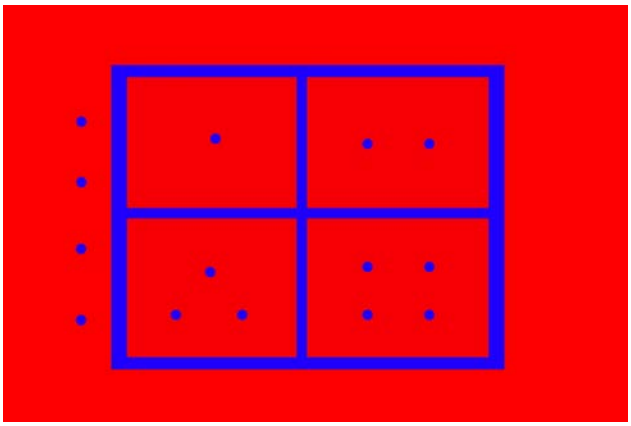

Figure C.1: *The pattern we used to create our alignment marks.*

1. Clean a $100mm$ silicon wafer with polished, thermally grown oxide, by spinning on Acetone and Isopropanol (in that order) at high speed.

2. Spin on organisilane primer at $4000rpm$ for $45s$.

3. Use a dropper to cover roughly half the surface of the wafer with Shipley 1813 photoresist. The resist should be dropped in the center of the wafer so that it spreads out

in a disc.

4. Spin the wafer at $4000rpm$ for $45s$. This should result in a resist thickness of $1.3\mu m$.

5. Bake the wafer at $115°C$ for $90s$.

6. Expose your indexing pattern by placing the pattern in blue on a red background which will react minimally with the photoresist (White and Black colors on the screen are projected with some blue light in them.) The timing can be easily controlled using a Microsoft PowerPoint© presentation.

7. In order to achieve good uniformity over the area of the exposure you should place the image at the bottom center of the slide. This is the area where the projector lamp exhibits the highest uniformity.

8. If you choose to use the pattern in figure C.1 the ideal settings are: the lines are $1pt$ and exposed for $65s$, while the dots should be placed on a separate slide so that they can be exposed for $75s$ at a size of $27pt$ through the $5x$ microscope objective.

9. Repeat the patterns as necessary on the surface of the chip. An effort should be made to group together 4-6 rectangles so as to allow for a more macroscopic indexing.

10. Develop the substrate in TMAH for $90s$.

C.2 Buffered Oxide Etch (BOE)

This recipe was developed by Mark Bachman [21] at UC Irvine. Hydrofluoric acid (HF) is extremely dangerous and should be treated with caution at all times. That said, this substance is widely utilized and when treated with proper caution is incredibly useful. HF will quickly eat at any glass therefore it needs to be stored in a Teflon or polypropylene

container. The following recipe will result in $160ml$ of 6:1 BOE. This mixture is extremely useful because the buffering ammonium ions prevent the HF from attacking photoresist. The resultant mixture will etch SiO_2 at a rate of approximately $2nm/s$.

1. Make sure you are wearing gloves, protective eye-wear, and an apron.
2. Weigh out $80g$ of NH_4F, which is a solid salt, and pour it into a beaker.
3. Pour $120ml$ of DI water into the salt. The solid will not dissolve immediately, however with stirring over a hotplate at $40°C$ it should be completely dissolved in 20 minutes.
4. Transfer the mixture to a polymer beaker and add $20ml$ of 49% HF
5. Transfer the resultant mixture to a polymer bottle and label it with "6:1 BOE. Danger: HF!"
6. Thoroughly rinse all beakers and graduated cylinders used in the process.

C.3 Argon Sputtering

1. Connect an Ar bottle to the fixture at the back of the Hummer II and allow Ar to flow.
2. Place your substrate on the sample area of the chamber at the top of the Hummer.
3. Switch the polarity to "etch" by turning the knob to the right of the chamber.
4. Power the rotary pump and make sure the "vent" and "leak" valves are fully closed.
5. Allow the chamber pressure to fall below $100mTorr$, then open the leak valve so that the pressure builds up to over $300mT$. Allow the Ar purge to continue for 5 minutes.
6. Adjust the leak valve so that the pressure falls back down to just over $100mT$ and stabilize it there.

7. Turn on the high voltage and turn the knob up until the current reads $15mA$.

8. After 5 minutes all the thinner pieces of graphite should have been etched away. Turn off the high voltage, then the vacuum system, and finally open the vent valve.

9. Once the chamber has been vented remove your sample and examine it under an optical microscope to check if the graphene layers have been etched away. If they remain repeat as necessary. After 10 minutes of etching the oxide will become significantly thinner.

C.4 High Temperature Furnace

1. You will need to dice the chip your sample is on so that it can fit in the quartz tube of the furnace you are using (The quartz tube in figure 4.4 is $1in$).

2. Using a long rod push your substrate into the center of the tube, so that it is right next to the thermocouple.

3. Close up the furnace, and program the temperature controller. I have been ramping up to $1000°C$ in 20 minutes, leaving it at that temperature for half-an-hour to an hour, and then turning off the heater.

4. Once the temperature falls below $500°C$ you can open up the furnace (carefully!) which will allow it to cool down much faster.

5. When the temperature drops to a few hundred degrees you can remove you substrate from the quartz tube and handle it with tweezers. If you then place it on a metal surface it will very quickly cool down to room temperature.

6. If you want to try for shorter times you can slide the quartz tube in and out of furnace so that you do not have to be limited by the cooling rate of the furnace.

7. One of the furnaces in Millikan is equipped to allow for oxygen flow during the run. This will allow you to operate at lower temperatures, but it will be much harder to slide the quartz tube.

List of Figures

Bibliography

[1] KS Novoselov, D. Jiang, F. Schedin, TJ Booth, VV Khotkevich, SV Morozov, and AK Geim. Two-dimensional atomic crystals. *Proceedings of the National Academy of Sciences*, 102:10451–10453, 2005.

[2] P. Blake, E. W. Hill, A. H. C. Neto, K. S. Novoselov, D. Jiang, R. Yang, T. J. Booth, and A. K. Geim. Making graphene visible. *Applied Physics Letters*, 91:063124, August 2007.

[3] K. S. Novoselov, A. K. Geim, S. V. Morozov, D. Jiang, Y. Zhang, S. V. Dubonos, I. V. Grigorieva, and A. A. Firsov. Electric field effect in atomically thin carbon films. *Science*, 306:666–669, October 2004.

[4] Y. Zhang, Y. W. Tan, H. L. Stormer, and P. Kim. Experimental observation of the quantum hall effect and berry's phase in graphene. *Nature*, 438:201–204, 2005.

[5] K. S. Novoselov, Z. Jiang, Y. Zhang, S. V. Morozov, H. L. Stormer, U. Zeitler, J. C. Maan, G. S. Boebinger, P. Kim, and A. K. Geim. Room-temperature quantum hall effect in graphene. *Science*, 315:1379, March 2007.

[6] J. S. Bunch, A. M. van der Zande, S. S. Verbridge, I. W. Frank, D. M. Tanenbaum, J. M. Parpia, H. G. Craighead, and P. L. McEuen. Electromechanical resonators from graphene sheets. *Science (New York, N.Y.)*, 315:490–493, 2007.

[7] D. A Areshkin and C. T White. Building blocks for integrated graphene circuits. *Nano Letters*, 7:3253–3259, 2007.

[8] S. V. Morozov, K. S. Novoselov, M. I. Katsnelson, F. Schedin, D. C. Elias, J. A. Jaszczak, and A. K. Geim. Giant intrinsic carrier mobilities in graphene and its bilayer. *Physical Review Letters*, 100:16602, 2008.

[9] S. A. Mikhailov and K. Ziegler. New electromagnetic mode in graphene. *Physical Review Letters*, 99:016803, July 2007.

[10] E. Rollings, G. H Gweon, S. Y. Zhou, B. S. Mun, J. L. McChesney, B. S. Hussain, A. V. Fedorov, P. N. First, W. A. de Heer, and A. Lanzara. Synthesis and characterization of atomically thin graphite films on a silicon carbide substrate. *Journal of Physics and Chemistry of Solids*, 67:2172–2177, 2006.

[11] J. W. Evans, P. A. Thiel, and M. C. Bartelt. Morphological evolution during epitaxial thin film growth: Formation of 2d islands and 3d mounds. *Surface Science Reports*, 61:1–128, 2006.

[12] A. K. Geim and A. H. MacDonald. Graphene: Exploring carbon flatland. *Physics Today*, 60:35–41, August 2007.

[13] I. W. Frank, D. M. Tanenbaum, A. M. van der Zande, and P. L. McEuen. Mechanical properties of suspended graphene sheets. *Journal of Vacuum Science & Technology B: Microelectronics and Nanometer Structures*, 25:2558, 2007.

[14] L. Yang, M. L. Cohen, and S. G. Louie. Excitonic effects in the optical spectra of graphene nanoribbons. *Nano Letters*, 7:3112–3115, October 2007.

[15] K. S. Novoselov, A. K. Geim, S. V. Morozov, D. Jiang, M. I. Katsnelson, I. V. Grigorieva, S. V. Dubonos, and A. A. Firsov. Two-dimensional gas of massless dirac fermions in graphene. *Nature*, 438:197–200, November 2005.

[16] T. W. Odom, J. L. Huang, P. Kim, and C. M. Lieber. Structure and electronic properties of carbon nanotubes. *Journal of Physical Chemistry B*, 104:2794–2809, April 2000.

[17] Z. F. Wang, Q. W. Shi, Q. X. Li, X. P. Wang, J. G. Hou, H. X. Zheng, Y. Yao, and J. Chen. Z-shaped graphene nanoribbon quantum dot device. *Applied Physics Letters*, 91:053109, July 2007.

[18] M. Y. Han, B. Ozyilmaz, Y. B. Zhang, and P. Kim. Energy band-gap engineering of graphene nanoribbons. *Physical Review Letters*, 98:206805, May 2007.

[19] Khunal Ghosh. Electronic band structure of carbon nanotubes, 2005.

[20] J. D Musgraves, B. T Close, and D. M Tanenbaum. A maskless photolithographic prototyping system using a low-cost consumer projector and a microscope. *American Journal of Physics*, 73:980, 2005.

[21] Mark Bachman. Buffered oxide etch, 2001.

[22] A. Gupta, G. Chen, P. Joshi, S. Tadigadapa, and P. C. Eklund. Raman scattering from high-frequency phonons in supported n-graphene layer films. *Nano letters*, 6:2667–2673, December 2006.

[23] A. C. Ferrari, J. C. Meyer, V. Scardaci, C. Casiraghi, M. Lazzeri, F. Mauri, S. Piscanec, D. Jiang, K. S. Novoselov, S. Roth, and A. K. Geim. Raman spectrum of graphene and graphene layers. *Physical Review Letters*, 97:187401, November 2006.

[24] D. Graf, F. Molitor, K. Ensslin, C. Stampfer, A. Jungen, C. Hierold, and L. Wirtz. Spatially resolved raman spectroscopy of single- and few-layer graphene. *Nano letters*, 7:238–242, February 2007.